Identifying airborne snow metamorphism with stable water isotopes

Sonja Wahl[1,2], Benjamin Walter[3], Franziska Aemisegger[4], Luca Bianchi[1], Michael Lehning[1,3]

[1]CRYOS, School of Architecture, Civil and Environmental Engineering, EPFL, Sion 1950, Switzerland
[2]University of Bergen and Bjerknes Centre for Climate Research, Bergen 5006, Norway
5 [3]WSL-Institute for Snow and Avalanche Research SLF, Davos Dorf, 7260, Switzerland
[4]Institute for Atmospheric and Climate Science, ETH Zürich, Zürich, 8092, Switzerland

Correspondence to: Sonja Wahl (sonja.wahl@uib.no)

Abstract.

Wind-blown snow is a frequent phenomenon in high-elevation and polar regions which impacts the surface energy and mass
10 balance of these areas. Loose surface snow gets eroded and transported by wind which influences the snow particle's
physical properties (size, shape, optical properties) that determine the characteristics of the emerging wind-impacted
snowpack layer. During airborne snow transport, the governing processes are happening on the micro-scale, while the
particles are transported over long distances. The unfolding processes and the evolution of the particle's physical properties
are thus difficult to observe in-situ. Here we used cold-laboratory ring wind tunnel experiments as an interim solution to
15 study the governing processes during airborne snow transport with stable water isotopes as tracers for these micro-scale
processes. Repeated analysis of airborne-sampled snow by micro-computed tomography (μCT) documented a growing and
rounding of snow particles with transport time with a concurrent decrease in specific surface area. Stable water isotope
analysis of airborne snow and water vapour allowed us to attribute this evolution to the process of airborne snow
metamorphism. The changes observed in the snow isotopic composition showed a clear isotopic signature of metamorphic
20 deposition, which requires particle-air temperature gradients. These results question the validity of the thermal equilibrium
assumption between particles and air inside the saltation layer of wind-blown snow events where the conditions are similar
to the ones found in the wind tunnel. Our results thus refine the understanding of the governing processes in the saltation
layer and suggest that the snow's isotopic composition can inform on local wind-blown snow events as the original snow
isotope signal gets overprinted by airborne snow metamorphism. Thus, airborne snow metamorphism has the potential to
25 influence the climate signal stored in snow and ice core stable water isotope records.

1 Introduction

The phenomena of blowing and drifting snow are frequently observed in snow-covered territory such as polar and alpine
regions (Yang et al., 2023; Wagner et al., 2022; Walter et al., 2020). Previously accumulated snow is mobilized and
redistributed by wind which affects both the surface energy and mass balance of the region and feeds back on snow
30 accumulation patterns. In the context of intense climate change in the cold climate zones around the globe, it is thus critical

to understand the underlying physical processes of wind-blown snow events to accurately model and predict future snow accumulation changes in these regions and their feedback on the climate system.

Wind-driven aeolian transport of snow can be classified into drifting snow close to the ground (~2 m) and blowing snow further aloft. The dominant snow particle transport modes are creep and saltation during drifting snow, and suspension during blowing snow events (Melo et al., 2022; Bagnold, 1941). Both transport regimes can coexist which motivates the terminology of a saltation and suspension layer in aeolian snow clouds (Nemoto and Nishimura, 2004).

The apparent effect of wind-blown snow is the redistribution of snow mass, which, depending on the surrounding topography and wind regime, can form snow surface structures such as ripples, dunes (Sommer et al., 2018a; Amory et al., 2016; Filhol and Sturm, 2015) and cornices (Yu et al., 2023). On glaciers and ice sheets snow redistribution also directly affects the surface mass balance when snow is blown off the ice margins, although this contribution is small (Palm et al., 2017). More importantly, wind-blown snow contributes negatively to the surface mass balance by enhancing sublimation of snow (Gerber et al., 2023; Sigmund et al., 2021; Palm et al., 2017). Concurrently, enhanced sublimation during wind-blown snow events leads to enhanced energy loss through a near-surface latent heat flux, which affects the near-surface energy balance and can in turn negatively feedback, or self-inhibit, the sublimation process by lowering the air temperature and increasing the relative humidity of the surrounding air (Amory and Kittel, 2019). Apart from these direct impact pathways on the surface energy balance during actual aeolian snow transport, wind-blown snow also indirectly affects the surface energy balance after the airborne snow has settled on the ground. This post-event influence is due to the modification of the particle size and shape of airborne snow particles during wind-blown snow events. We will use the term physical properties of particles (PPP) in analogy to the physical properties in ice core studies when referring to snow particle shape, size and morphology. After settling, the PPP define energy balance-relevant characteristics of the resulting snowpack such as albedo (Domine et al., 2006), emissivity (Hori et al., 2013), density and specific surface area (SSA) (Proksch et al., 2015; Schleef et al., 2014b). Previous studies (Walter et al., 2023; Sommer et al., 2017) have shown that wind-driven aeolian transport of snow significantly affects the microstructure of the ultimately deposited surface snow, i.e. density increase and SSA decrease are intensified under the influence of wind. A resulting wind-blown snow layer is typically characterized by small, broken or abraded, closely packed and well-sintered particles (Fierz et al., 2009). Mechanisms that control the modification of the PPP and thus the resulting snowpack characteristics can be grouped in mechanical processes such as particle fragmentation, abrasion (Comola et al., 2017; Gromke et al., 2014; Clifton et al., 2006) and aggregation (Lo and Passarelli, 1982) or in thermodynamic (hereafter metamorphic) processes, such as sublimation at snow particle surfaces (Schmidt, 1982; Thorpe and Mason, 1966) and vapour deposition (resublimation) on the suspended snow particle (Sigmund et al., submitted; Yamaguchi et al., 2019; Sharma et al., 2018). In this context, Walter et al., (2023) first introduced the term "airborne snow metamorphism" which summarises the multiple cycles of sublimation and vapour deposition on the suspended snow particle resulting in modifications of the snow particle size and shape during particle transport by wind in analogy to isothermal and temperature-gradient metamorphism inside a stationary snowpack (Schleef et al., 2014b; Pinzer and Schneebeli, 2009b; Colbeck, 1982). However, the relative importance of the individual processes involved and their combined effect on the

snow microstructure is still unknown due to missing observations. Snowpack or climate models that include wind-blown snow modules thus rely on field-based empirical parameterizations when incorporating wind-blown snow effects on snowpack characteristics, because the physical process understanding is limited (Walter et al., 2023).

In-situ observations of changes in the PPP during wind-blown snow events are difficult due to the micro-scale nature and short timescales on which these processes evolve, while the particles cover large distances on their airborne trajectories. Thus, in-situ observations are limited to point measurements within the snow cloud (Nishimura et al., 2014; Nishimura and Nemoto, 2005) or pre- and post-event monitoring of the snowpack characteristics (Walter et al., 2023). Field measurements are the foundation for wind-blown snow parameterizations that are currently implemented in snowpack and climate models (Vionnet et al., 2012; Liston et al., 2007; Lehning et al., 2002). As an approach to circumvent the difficulties of multiple unconstrained environmental variables during in-situ field observations, controlled laboratory experiments using straight wind tunnels (Nishimura et al., 2014; Wever et al., 2009) or ring-shaped wind tunnels with infinite fetch (Walter et al., 2023; Sommer et al., 2018b) have been used successfully to systematically validate model parameterizations. Additionally, shadowgraphy imaging based on high-speed camera recordings (Gromke et al., 2014) has been applied in wind tunnel experiments to investigate the vertical distribution of snow particle size and number. However, this method does not allow accessing information on the evolution of PPP and thus the differentiation between mechanical (fragmentation, aggregation and abrasion) and metamorphic (sublimation and vapour deposition) drivers. Consequently, means to constrain the underlying governing equations of the PPP evolution during airborne snow metamorphism are still missing due to the nature of the processes unfolding on the difficult-to-observe micro-scale.

As direct observations of the individual airborne snow particles are currently impossible, indirect methods such as the monitoring of proxy variables are key to being able to disclose metamorphic processes happening on the micro-scale in macro-scale variables. For snow processes, such a proxy can be the abundance of stable water isotopologues (hereafter simplified to "water isotopes") $H_2^{16}O$, $H_2^{18}O$ and $^2H^1H^{16}O$ in a sample. Due to their predictable partitioning, i.e. *fractionation* into the vapour and ice phase during phase changes (i.e. water vapour deposition and sublimation), stable water isotopes are powerful tracers, which allow to identify and quantify the impact of metamorphic processes on the PPP (Mook, 2000). Ideally, stable water isotope measurements comprise both (solid and gas) phases to fully constrain the isotopic fractionation during phase change processes. Stable water isotopes are measured as abundance ratio R of the rare (i.e. $^1H_2^{18}O$ and $^2H^1H^{16}O$) to the most abundant $^1H_2^{16}O$ isotope and are commonly reported as δ-values referenced against an international standard (equal to the isotope ratio of the mean ocean water) and given in ‰ (Craig, 1961b; Mook, 2000):

$$\delta^{18}O = \frac{R^{18}O_{sample}}{R^{18}O_{standard}} - 1 \ (\cdot 10^3 \ ‰) \tag{1}$$

Isotopic fractionation is temperature (T) dependent and empirically well established for equilibrium fractionation processes between vapour and ice (Majoube, 1970; Merlivat and Nief, 1967). For non-equilibrium processes, i.e. processes including a

humidity gradient ($RH \neq 1$), the net fractionation between two phases deviates from the pure equilibrium fractionation factor α_{eq} by a non-equilibrium (sometimes also termed kinetic) fractionation factor α_k that is due to different molecular diffusivities

100   for the different isotopes (Merlivat, 1978). The effective fractionation factor of a phase change is thus defined as:

$$\frac{R^{18}O_{ice}}{R^{18}O_{vapour}} = \alpha_{net}(\mathrm{T}, \mathrm{RH}_s) = \alpha_{eq}(\mathrm{T}) \times \alpha_k(\mathrm{RH}_s) \tag{2}$$

Where RH_s is the relative humidity normalised to surface saturation and defines the humidity gradient. Usually $\alpha_{net} > 1$, which shows that the resulting ice phase is enriched in the rare water isotope compared to the relatively depleted vapour phase, hence $\delta^{18}O_{ice} > \delta^{18}O_{vapour}$. However, deposition under supersaturation conditions ($RH_s > 1$) can lead to strong non-

105   equilibrium fractionation, such that $\delta^{18}O_{ice} < \delta^{18}O_{vapour}$ (Jouzel and Merlivat, 1984). Equation (1) and (2) can be written analogously for $^1H^2H^{16}O$ with the notation δD used onwards. From both isotopes the second order variable d-excess can be derived as $d - excess = \delta D - 8 \times \delta^{18}O$ (Craig, 1961a). The slope 8 originates from the eight-fold stronger fractionation of $^2H^1H^{16}O$ compared to $H_2^{18}O$ under equilibrium conditions. Per definition, this variable will not change under pure equilibrium conditions, and changes in d-excess thus indicate non-equilibrium fractionation processes. Note that, due to the

110   non-linearity of the δ-scale, under very depleted conditions, this assumption does not hold (Dütsch et al., 2017). An additional concept to understand and predict isotope behaviour is the analysis of the out-of-equilibrium state, i.e. the *disequilibrium* in isotopic composition between two phases of water similar to the analysis by Aemisegger et al. (2015) or Wahl et al. (2022). For this, the temperature-dependent equilibrium state between two phases is compared against the actual isotopic composition of the respective phase. The difference between the equilibrium and the actual isotopic composition is

115   called *disequilibrium* and it describes if a water entity is more enriched or depleted compared to the equilibrium state. This analysis can inform on the expected evolution during mixing of water entities of the original and newly produced phase and help to reconcile isotope signal behaviour in transient conditions.

This paper aims to characterise airborne snow metamorphism and its effect on the temporal evolution of PPP during wind-blown snow events for the first time through the lens of stable water isotopes. To this end, we set up cold-laboratory

120   experiments using a ring wind tunnel to simulate wind-blown snow events under controlled conditions and for long transport durations (Section 2). We monitored the co-evolution of PPP and the isotopic composition of both aeolian snow and water vapour inside the ring wind tunnel. From these observations, we deduce the underlying physical processes that are responsible for changes in PPP and relate them to the ambient atmospheric conditions (Section 3). We discuss the significance of our findings for resulting snowpack characteristics and the modeling and calculation of energy and mass

125   balance of wind-blown snow events and we reflect on the implications of our findings for the climate signal imprinted in the snow isotopic composition (Section 4).

2 Materials and Methods

All experiments were conducted at the cold-laboratory facilities of the WSL institute for snow and avalanche research, SLF
130   in Davos, Switzerland. The experiments were performed in two periods, one from 09.–13.01.2023 and the other from 11–
31.05.2023. In the following, an overview of the 19 experiments and the sampling protocol is given and the experimental
setup is described.

2.1 Cold-laboratory wind tunnel experiments

The experiments aimed to simulate wind-blown snow transport in the ring wind tunnel for long transport times while
135   monitoring snow properties and environmental variables to observe changes and identify the corresponding governing
mechanisms. For this, 600 g of fresh snow with known initial PPP and isotopic composition were introduced to the wind
tunnel at an initial wind speed of ~8.5 m s^{-1} and airborne snow was then repeatedly sampled out of the airstream until no
more snow was in suspension.

To keep the experiments' initial conditions as repeatable and reproducible as possible we used artificially produced snow
140   from SLF's snowmaker (Schleef et al., 2014a) which produces nature-identical snow from tab water. The snowmaker was
situated in the same cold-laboratory but was not in operation during the experiments. The snow was produced at an air
temperature of -20 °C and a water bath temperature of +30 °C yielding dendritic and hollow column crystals with very low
density (45–80 kg m^{-3}) and high SSA (50–70 mm^{-1}) (Walter et al., 2023). The produced snow was stored at -20 °C for a
maximum of four days before it was used for the experiments. Care was taken to equilibrate the snow to the wind tunnel air
145   temperature for 30–60 min before the start of the experiment. The snow was well mixed, its temperature measured, and three
replicate samples of 10 g were taken before the introduction of the snow to the wind tunnel to estimate the initial isotopic
composition. The mean of these three samples serves as the initial condition snow isotope value for each experiment.
Depending on storage time and mixing success, the three initial snow samples agreed to within a range of standard
deviations (std) of 0.01–0.66 ‰ for δ^{18}O, 0.0–2.8 ‰ for δD and 0.1–2.5 ‰ for d-excess with a mean std of 0.12 ‰ for δ^{18}O,
150   0.7 ‰ for δD and 0.6 ‰ for d-excess within the set of 19 experiments.

At the start of the experiments, the wind tunnel was closed before the snow was prepared for introduction. After the
conditions inside the wind tunnel had reached an equilibrium, the wind generation was initiated quickly reaching wind
speeds >8 m s^{-1}, which is well beyond the threshold wind speed for snow movement and ensures that snow is transported in
suspension (Yu et al., 2023; He and Ohara, 2017). Shortly after reaching the maximum wind speed, the snow was added to
155   the wind tunnel in small batches through a port in the ceiling within a short time window of 2–5 min. After the snow
introduction to the wind tunnel, a part of the snow was not kept in suspension due to the geometry of the flow field in the
wind tunnel (Sommer et al, 2017). Some snow accumulated in the curved section underneath the propellor location. In
addition to this early and permanent deposition of snow, a saltation layer with a height of approximately 5–10 cm (Walter
al. 2023, Yu et al., 2023) formed in the wind tunnel where snow was continuously deposited and re-eroded. Importantly,

160   some part of the snow was permanently in suspension up to heights of 10–40 cm. Throughout the whole experiment and until all airborne snow particles had disappeared (due to sublimation or accumulation) the environmental conditions (temperature (T), wind speed (WS), relative humidity (RH)) and the vapour isotopic composition (δ_v) inside the wind tunnel were monitored using the sensors presented in the next section. Additionally, a small amount of snow (3–10 g) was sampled from the air several times during a single experiment using a Whirl-Pak® that was tied to a hand net frame. This sampling

165   tool was inserted into the wind tunnel through a hole in the wind tunnel ceiling and was moved up and down in the air stream covering the whole height of the wind tunnel until enough snow had been captured in the Whirl-Pak® for later water isotope analysis in the laboratory. During six experiments, part of the so-collected snow was transferred to specific sample holders for the analysis of particle shape, size and distribution using microcomputed tomography (µCT). Thereafter, the Whirl-Pak® was closed and stored at -20 °C until further preparation for shipment to the isotope laboratory facility. Once no snow was

170   left in the air column, the experiment was declared finished and the propellor was turned off. Two samples of the accumulated snow were taken right after the wind tunnel was opened: one from the surface layer and one from inside the accumulated snow. Before the start of a new experiment, the sealed wind tunnel was opened to the laboratory air to allow sublimation of vapour depositions on walls and ceiling and all leftover snow was cleaned out.

The temperature regime at which the experiments were conducted was regulated by adjusting the room temperature of the

175   laboratory. During the experiment runs, the air temperature inside the wind tunnel was observed to increase whereas the room temperature of the cold-laboratory was kept stable (±1 °C) by the laboratory climate control system. The source of this observed warming of the air within the wind tunnel during the experiment can be primarily attributed to the heat generation of the motor and propellor setup. A control run with a sealed but empty wind tunnel was performed to characterize the experiment setup behaviour without added snow. The measurements of this control run are presented in Fig. S1 of the

180   Supplementary Material (SM). It was identified that the precise position of the wind tunnel inside the laboratory with regard to the internal air-conditioning system played a major role in limiting the heating of the air inside the wind tunnel during the experiment. The heating was minimised when the wind tunnel was placed directly opposite the air conditioning system which allowed for the most effective air circulation in the cold-laboratory.

In total 19 experiments were conducted at different temperature regimes spanning a temperature range of -20 °C – -3 °C at

185   the start of the experiments. In two special cases, the laboratory temperature was increased or decreased during the experiment duration leading to pronounced warming (Experiment No 18, ΔT: +13.5 °C) or cooling (Experiment No 12, ΔT: -6 °C) in the wind tunnel. Details on the specific characteristics of each experiment are summarised in Table 1.

190

Table 1 The characteristics of the 19 ring wind tunnel experiments During the three experiments in January (grey shading) no water vapour isotopes were measured and the humidity increase (ΔH_2O) is estimated based on the RH sensors. (disc. = discarded)

Experiment		Snow	Snow samples	µCT scan	Duration	Average air temperature	ΔT	ΔH_2O	
No	Date	from date	#(#airborne)		min	°C	°C	g kg^{-1}	Pa
1	2023-01-12	2023-01-11	8(4)		157	-18.3	2.6	0.24	33
2	2023-01-13	2023-01-11	9(5)		138	-3.3	2.6	1.32	178
3	2023-01-16	2023-01-11	7(3)		101	-8.6	2.3	1.12	147
4	2023-05-11	2023-05-09	9(4)		70	-15.1	1.9	0.24	32
5	2023-05-12	2023-05-09	8(3)		49	-7.4	2.8	0.71	94
6	2023-05-23	2023-05-22	10(5)		119	-16.6	3.1	0.28	37
7	2023-05-23	2023-05-22	11(6)		137	-17.4	3.8	0.31	41
8	2023-05-24	2023-05-22	9(4)		85	-7.9	3.6	0.61	81
9	2023-05-24	2023-05-22	10(5)	x	87	-7.2	3.8	0.62	82
10	2023-05-25	2023-05-22	15(10)	(x) disc.	180	-2.9	2.6	1.15	154
11	2023-05-26	2023-05-22	10(5)		96	-4.0	2.5	0.74	100
12	2023-05-26	2023-05-22	13(8)	x	152	-7.0	-6.3	-0.81	-109
13	2023-05-28	2023-05-27	12(7)		128	-10.9	2.5	0.48	64
14	2023-05-28	2023-05-27	11(6)	x	112	-14.0	2.4	0.21	28
15	2023-05-29	2023-05-27	12(7)		113	-5.5	2.2	0.87	117
16	2023-05-29	2023-05-27	11(6)	x	103	-5.2	2.4	0.91	121
17	2023-05-30	2023-05-29	12(7)	x	158	-18.0	2.9	0.33	44
18	2023-05-30	2023-05-29	19(14)		88	-12.8	13.5	1.74	234
19	2023-05-31	2023-05-29	9(4)		62	-2.1	2.1	0.52	69

2.2 Instrumentation

2.2.1 Ring wind tunnel and setup

We used an existing ring wind tunnel (Fig. 1, Yu et al., 2023; Sommer et al., 2018b) that was placed in a cold-laboratory of the SLF. An outer and inner ring made of wood and plexiglass are placed on wooden planks a few centimetres above the laboratory floor forming a tunnel with a rectangular cross-section and dimensions of 50 cm height and ~20 cm width. The resulting oval ring has outer dimensions of 2.20 m length and 1.20 m width, and the removable lids can be attached to the wooden frame with metal locks. The wind tunnel was sealed against snow loss with the help of insulation material. However,

the tunnel is not fully air-tight and minor exchange with the laboratory air is inevitable. Wind is generated by an electrically motored two-blade propellor that accelerates the air at a height of approximately 40 cm in the wind tunnel. The wind tunnel is equipped with basic meteorological instrumentation in the *observation section* of the tunnel where the lid and walls are

205 made from plexiglass (Fig. 1). This is where *WS* is recorded by a *MiniAir60 (Schildknecht)* wind sensor at 37 cm height. *Hygroclips HC2-S* (*Rotronics*) measuring *RH* and *T* are installed at three heights (15 cm, 30 cm, 42.5 cm) and an additional *Pt100 (Mösch AG) T* sensor is installed at 3 cm. The *T* and *RH* sensors were calibrated in dedicated calibration runs. During these runs, they were placed close together and referenced against their mean readings in a range of -21.5 °C – -5 °C and 46 – 91 % to be comparable. For water vapour sampling, we installed a heated copper tube (OD ¼", ID 0.19") that was entering

210 the wind tunnel through a hole in the lid at the same *observation section.* The copper tube was bent such that its opening was oriented with the wind direction, looking downwind at a height of 47 cm in the wind tunnel. The tube then was fed through a connection hole in the laboratory wall and connected to a *KNF* membrane vacuum pump that was installed in the temperate surroundings outside the cold-laboratory. The tube was heated to about 5 °C above the cold-laboratory temperature and insulated with *Armaflex* insulation material to prevent condensation inside the tube. The flow rate inside the copper tube was

215 set to 200 mℓmin^{-1} and controlled by a *Sensirion* Mass Flow Controller of type *SFC5500-10SML.* The wind tunnel has four round holes with a 10 cm diameter in each curve that are closed with metal lids but allow access to the inside of the wind tunnel. Samples of airborne snow were taken through one of these holes.
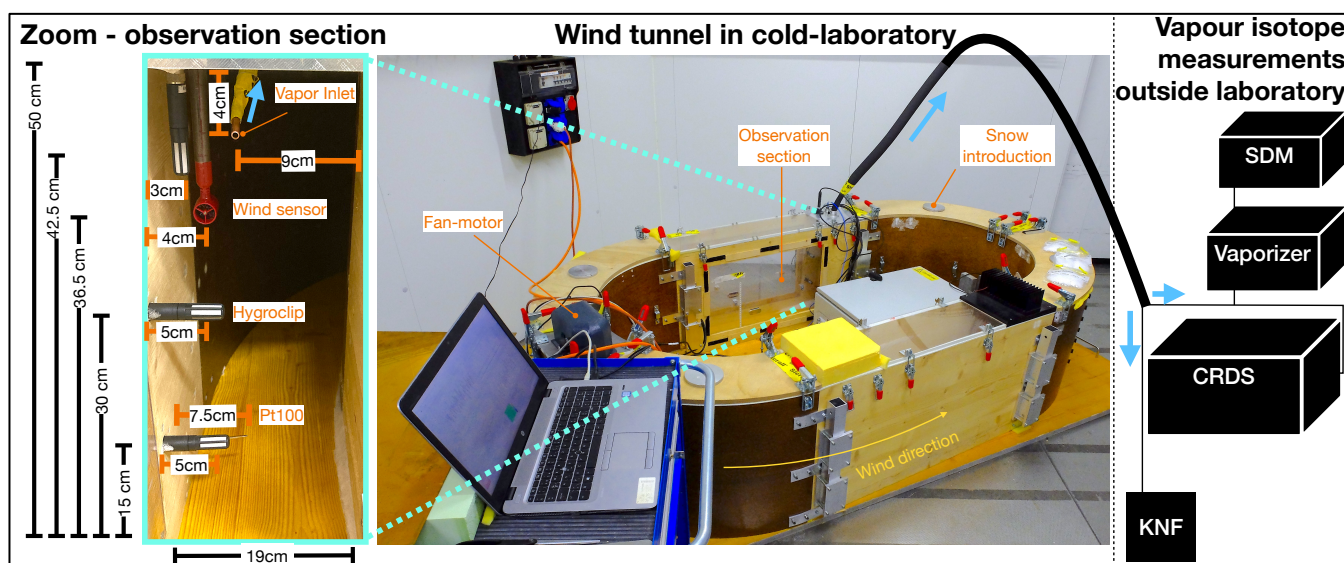
220 **Fig. 1 Wind tunnel setup.** In the centre, the ring wind tunnel is shown as it was installed in the cold-laboratory. A close-up of the observation section is shown on the left displaying the positions of the sensors that measured the environmental conditions inside the wind tunnel during the experiments. The vapour measurement setup including the Cavity Ring-Down Laser Spectrometer (CRDS) was installed outside the cold-laboratory and is shown schematically on the right. The KNF pump pumped air at a low flow rate of 200 mℓmin^{-1} out of the wind tunnel (blue arrows) to the CRDS for continuous real-time analysis of the water vapour and its isotopic composition. During

225 CRDS calibrations, the standard delivery module (SDM) and vaporiser generated a vapour stream of constant humidity and isotopic composition to be measured by the CRDS.

2.2.2 Stable water isotope measurements

During the experiments, we measured the water vapour inside the wind tunnel continuously and sampled drifting and blowing snow periodically for stable water isotope analysis of both water phases.

230 **Isotopic composition of the water vapour**

For analysing the isotopic composition of the water vapour, a cavity ring-down laser spectrometer (CRDS) of type Picarro *L2130-i* was connected to the copper tube outside the laboratory at stable room temperature (~18 °C) and drew in air at the instrument's flow rate of 30 mℓ min^{-1} through the connected vaporiser. The total length of the copper tube between the inlet in the wind tunnel and the entry to the vaporiser was 4.6 m for the first 5 experiments and 6.1 m after repositioning the wind

235 tunnel in the laboratory. The time delay between a signal occurring in the wind tunnel before it was recorded by the CRDS was experimentally determined to be 38 s and 50 s, respectively. As we expect no abrupt jumps in the vapour isotopic composition from the processes in the wind tunnel but rather smooth transitions this lag time is acceptable. The meteorological and water vapour readings were synchronised while accounting for this time lag during data post-processing. The recorded vapour measurements were calibrated following standard procedures:

240 The humidity readings of the CRDS were calibrated with a Li-610 dew point generator in the temperature range between 0 °C and 20 °C, with an emphasis on the range between 0 °C and 2.5 °C. In total, 14 calibration pulses of constant (max std ±16 ppmv) humidity between 20–30 min were generated with the Li-610 and calibrated against the respective saturation vapour pressure following Murphy and Koop (2005). As independent calibration validation, all CRDS humidity measurements were compared to the humidity measurements of the highest *Hygroclip* when both sensors were measuring at

245 the same time. Both measurement techniques yield specific humidity (g kg^{-1}) readings that agree reasonably well with a slope of 0.98, an offset of 0.04 g kg^{-1} and an R^2 of 0.99 at p<0.001.

The water vapour isotope measurements were first corrected for the humidity-dependency of the CRDS instrument (Aemisegger et al., 2012) and afterwards calibrated against the VSMOW-SLAP scale. The instrument-specific humidity-dependency curve was established using a standard delivery module (SDM) of Picarro by injecting vapour of known isotopic

250 composition at different humidity levels to the CRDS through the vaporiser of model *V1102-i* in the week prior to the experiments. Since the range of the expected isotopic composition of water vapour was narrow, only one humidity-dependency curve was established for a standard water with isotope values close to the expected values (PCD: δ^{18}O = -20.87 ‰, δD = -169.5 ‰). This water standard was measured in a humidity range between 500–18000 ppmv with 16821±44 ppmv as the reference normalisation humidity level calculated from 10 plateaus. The data points for the humidity-dependency

255 calibration curves were calculated from 15–25 min of continuous CRDS data at constant (max ± 190 ppmv, mean std of 91 ppmv) humidity levels and the calibration curves for both isotopes were established as orthogonal least-square fit of form $y = \frac{a}{x} + bx + c$ to a total of 115 data points (SM Fig. S2) following Weng et al. (2020).

For the normalisation to the VSMOW-SLAP scale two standard waters (MP: δ^{18}O = -11.12 ‰, δD = -79.8 ‰, GRIP: δ^{18}O = -34.14 ‰, δD = -265.0 ‰) bracketing the expected vapour isotopic composition were vapourised and injected

260   to the CRDS by the SDM once a day, first at a high humidity level of 26000 ppmv for 15 min to reduce memory effects and afterwards at a constant (max std 190 ppmv, mean std 99 ppmv) humidity level of 16770 ± 354 ppmv (mean and std of all 36 accepted calibration pulses). Continuous measurements of 16–25 min were averaged to obtain the calibration point for each day and each standard water. Since no instrument drift was observed during the laboratory campaign all water vapour measurements were calibrated with the same calibration data set. This is consistent with other campaigns during which

265   negligibly small drifts of the CRDS instrument were observed (Bailey et al., 2023). The calibration data set was generated by calculating a linear least-square fit to all 36 accepted calibration pulses of which 21 were of standard water MP and 15 of standard water GRIP obtained from calibration runs on 13 days. The water standards for the SDM had to be refilled once during the campaign which resulted in small changes in the standard waters isotopic composition that were accounted for during the normalisation. All used sets of standard water were analysed for their isotopic composition at the Hydrology

270   laboratory of the University of Freiburg. We estimate the uncertainty of the standard water from replicate samples taken a minimum of five days apart from the SDM which had an absolute offset of ≤ 0.03 ‰ for $\delta^{18}O$ and ≤ 0.3 ‰ for δD. The humidity-corrected and calibrated 1-s vapour measurements were resampled to 3-min averages. The uncertainty associated with the precision of the vapour isotope data is estimated as standard error of the mean of the 3-min averages.

The snow samples were melted in the air-tight closed Whirl-Paks®, filtered with a 0.2 µm filter (VWR Nylon-membrane, 25

275   mm) and 1.5 mℓ of the sample was transferred to 2 mℓ glass vials and sealed. The samples were sent to and analysed at the stable water isotope laboratory of the Paul Scherrer Institut in Villigen, Switzerland following established laboratory procedures with an uncertainty of the individual snow sample isotopic composition of <0.1 ‰ for $\delta^{18}O$ and <0.5 ‰ for δD (Avak et al., 2019) which yields an uncertainty of 0.9 ‰ on d-excess.

2.2.3 Micro CT scanning

280   Micro-computed tomography (µCT) 3D microstructure measurements of the airborne snow samples were performed to obtain information on the evolution of the SSA and the particle size distributions of the snow during the experiments. A small portion (≈ 1 cm²) of the periodically sampled snow was filled in a cylindrical µCT sample holder with a diameter of 15 mm. The measurements were performed using a Scanco® CT-40 scanner (e.g. Heggli et al., 2011; Pinzer and Schneebeli, 2009a). A small sample holder was chosen to obtain a high 3D microstructure resolution (voxel size of 8 µm) and thus derive

285   accurate measurements of the SSA and particle size distributions. For the binary segmentation, the energy-based segmentation procedure presented by Hagenmuller et al. (2013) was used. A marching cubes approach (Hagenmuller et al., 2016) was used for calculating the SSA from the segmented µCT images. A metric for the particle size distribution can be derived from the µCT images by filling the 3D ice matrix with inscribed spheres of different diameters d (Hildebrand and Rüegsegger, 1997).

3 Results

In the following we present the evolution of the PPP during the wind-blown snow experiments (Section 3.1), followed by the results of the evolution of the snow and vapour isotope signals after calibration and post-processing (Section 3.2).

3.1 The evolution of the snow's physical properties during aeolian transport

During six of the 16 experiments conducted in May 2023, the airborne snow samples were analysed for their PPP through measurements of specific surface area (SSA) and sphere size distribution analysis using a µCT scanner. The results of experiment No. 10 had to be discarded as the snow was stored at -2 °C for too long before the samples were measured which led to distorted µCT results. In the five remaining experiments, the SSA of the last snow sample was reduced to 35–70 % of the initial SSA after being transported in the wind tunnel for 1.25–2.5 h. The observed SSA decrease follows an exponential decay as a function of transport time (Eq. 3, Fig. 2 (a)) in agreement with previous SSA decay observations (Cabanes et al., 2003).

$$SSA(t) \; = \; (SSA_0 - c) \, e^{-\alpha t} + c \qquad\qquad (3)$$

with t for transport duration, α for decay rate and c a parameter for the non-zero asymptote. Neither α nor c show a simple dependency on the temperature regime of the experiment.

The sphere sizes detected in the initial and airborne snow samples can be described with a two-parameter gamma distribution similar to the expected particle size distributions in wind-blown snow (Budd, 1966; Schmidt, 1982; Clifton et al., 2006). The evolution of the sphere size distribution in all experiments followed a general coarsening pattern. As shown in Fig. 2 (b), the initial snow samples (fresh snowmaker snow) show a distinct peak at ~30–40 µm sphere size with the largest detected sphere sizes reaching 100–150 µm. With time, both the distribution peaks and maximum values gradually shift towards larger sphere sizes. The smallest sphere sizes detected in the fresh snow (~10 µm) had disappeared in the first airborne samples. However, small sphere samples (~20 µm) are universally detected in all samples taken, i.e. there is only a marginal shift in minimum sphere sizes detected with transport time. Hence, airborne transport leads to a broadening of the distributions. After >80 min of airborne transport the biggest particles have sphere sizes of >175 µm, reaching 200 µm or larger for the last airborne samples taken in each experiment. By the end of each experiment, the most abundant sphere sizes had shifted to 60–75 µm. Interestingly, the samples taken from the accumulated snow show a difference in the distribution of samples taken from the inner part vs. the surface layer. The sample from the surface layer ("acc_out", Fig. 2) shows a similar sphere size distribution as the airborne samples towards the end of the experiment, whereas the snow from within the accumulation layer ("acc_in", Fig. 2) typically shows a distribution more closely resembling the early airborne snow samples. This supports our assumption that snow that is deposited early during the experiment remains in the accumulated snow layer and that snow that is sampled from the airstream can be regarded as "active snow", i.e. it was transported either in saltation or suspension throughout the entire experiment duration. Note that density measurements of snow collected from an airstream are meaningless and are thus not shown.
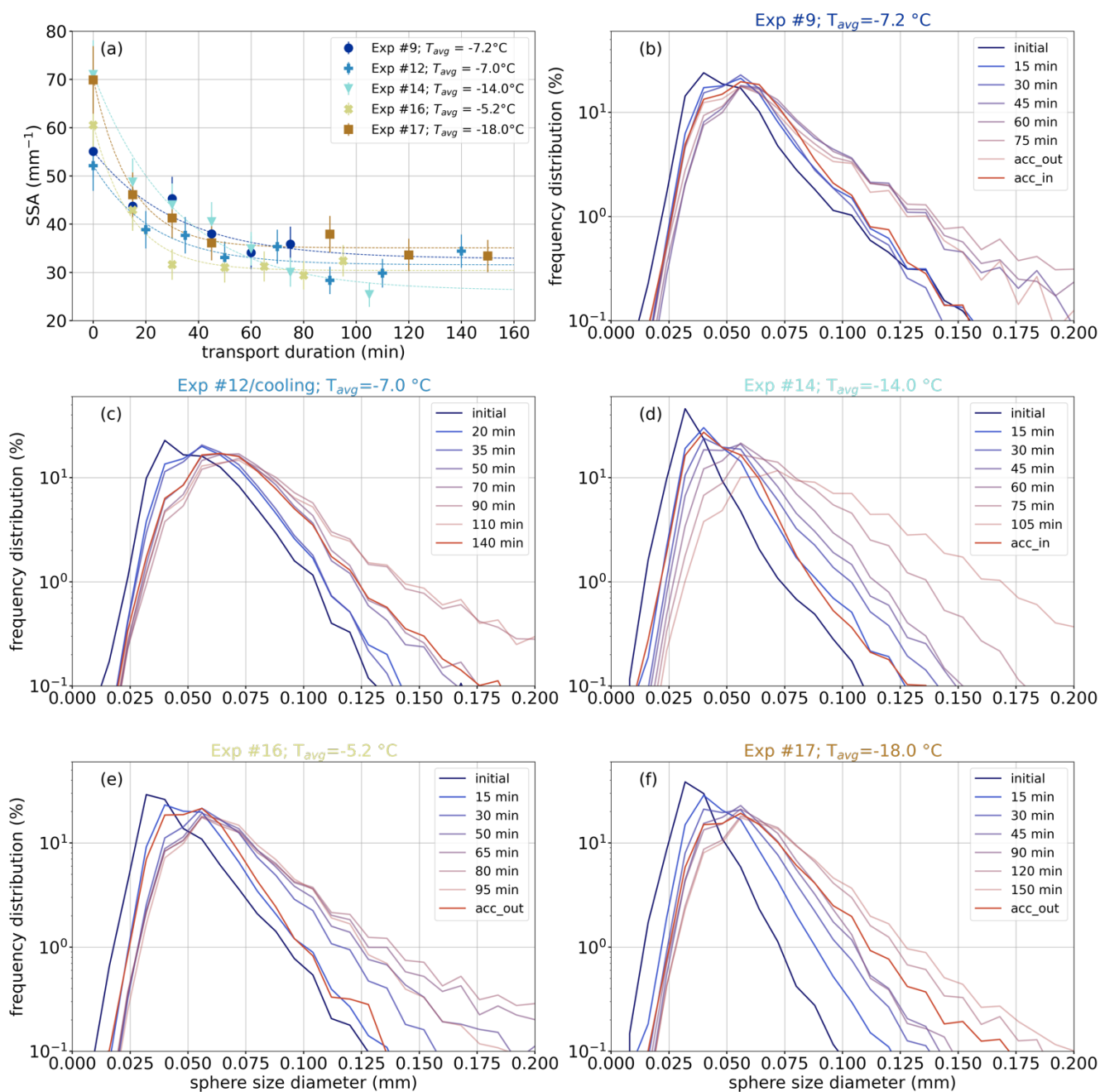
Fig. 2. The results of the µCT scans of five experiments. Panel (a) displays the decrease of SSA values with transport time in all five experiments at different temperature regimes. Dashed lines are exponential fits of Eq. 3 to the data points. Panel (b)–(f) show the corresponding sphere size distributions for one experiment each that serves as a measure for representative snow particle size. Each distribution is calculated from one snow sample and the colour corresponds to the time after snow introduction. "acc" samples were scraped off the snow accumulation in the wind tunnel. "acc-out" was taken from the surface layer and "acc_in" from the innermost part of the accumulated snow.

3.2 The isotopic signature of wind-blown snow experiments

330 To identify the underlying process responsible for the changes in the physical properties during aeolian transport, the evolution in the water isotope signal of the snow was obtained from discrete snow sampling at regular time intervals after the snow introduction to the wind tunnel and the vapour isotopic composition in the wind tunnel was measured continuously.

3.2.1 Changes in the snow isotopic composition

  The snow isotopic composition changed with time during aeolian transport. Figure 3 shows the change in isotopic
335 composition between the initial snow (mean of three samples) and the first airborne sample in panel (a), (b) and (c) and the maximum observed change between initial and airborne snow in panel (d), (e) and (f) for δ^{18}O, δD and d-excess, respectively. Just after the snow introduction, the majority of the experiments show a significant enrichment in the snow δ^{18}O value (15/19) and a decrease in the d-excess value (14/19). For δD, only 5/19 experiments show a significant enrichment. In all other experiments, the observed changes in the first airborne snow sample are within the uncertainty
340 limits of the calculated difference and thus not significant. The snow isotopic composition evolved further during aeolian transport.

  The general pattern of maximum observed changes between initial and airborne samples that are significant are a δ^{18}O enrichment (15/19) and a d-excess decrease (17/19). Three experiments show a reverse behaviour of significant δ^{18}O depletion, and one experiment shows a d-excess increase. For δ^{18}O the observed range of maximum change within one
345 experiment is -0.88 ‰ – 1.47 ‰, with a mean of 0.28 ‰ ± 1 std of 0.5 ‰. The range of d-excess changes is -6.1 ‰ – 1.3 ‰ with a mean change of -2.5 ‰ ± 1.6 ‰. For δD, the maximum isotope change recorded is almost evenly distributed between enrichment (9/19) and depletion (7/19) cases and three recorded changes fall within the range of measurement uncertainty. The observed range spans changes between -5.7 ‰ – 5.7 ‰ with mean -0.0 ‰ ± 2.7 ‰. Both the cooling (No. 12, ΔT: -6.3 °C) and the warming (No. 18, ΔT: +13.5 °C) experiment follow the general pattern of δ^{18}O enrichment and d-
350 excess decrease in the first airborne snow sample which intensifies during the experiments. For δD, both experiments show a significant enrichment only after the first snow sampling time. During the warming experiment, 14 airborne snow samples were taken which allows a robust trend analysis for this experiment. Including the initial mean isotopic composition and accounting for the uncertainties, the trends for snow isotopic evolution have positive slopes (m) for δ^{18}O (m=0.006 ‰ min^{-1}, p=0.000) and δD (m=0.011 ‰ min^{-1}, p=0.091), and a negative slope for d-excess (m=-0.049 ‰ min^{-1}, p=0.002).
355 No general, simple dependency between observed isotopic changes and average temperature, net sublimation, transport duration nor initial isotopic composition can be identified. Note that the net increase in humidity correlates positively with the average experiment temperature as expected by the Clausius-Clapeyron relationship (Fig. 3).
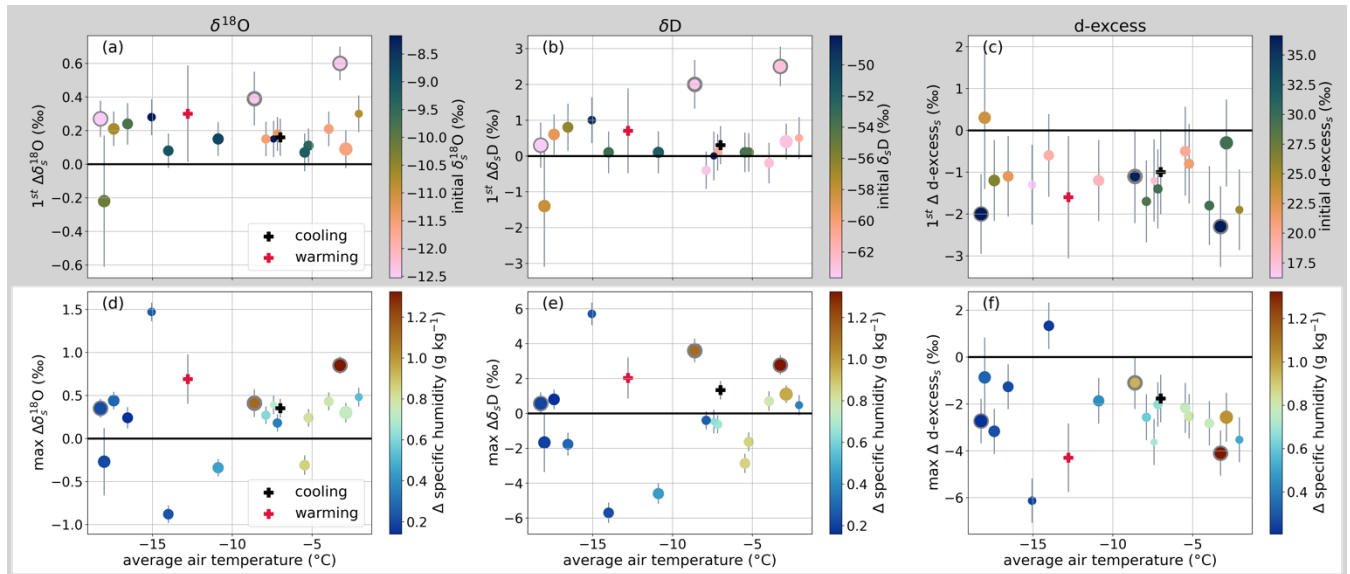
Fig. 3: Overview of recorded changes in snow isotopic composition during the 19 different experiments. The upper row (grey
background) shows the change in snow isotopic composition (δ_s) between the average initial snow and the first airborne snow sample
($1^{st} \Delta\delta_s^{18}O = \delta_s^{18}O_{1st} - \overline{\delta_s^{18}O_{initial}}$). The lower row shows the maximum observed change between average initial and airborne snow
(max $\Delta\delta_s^{18}O = \delta_s^{18}O_j - \overline{\delta_s^{18}O_{initial}}$, j = airborne sample with largest deviation from initial snow). Changes in $\delta^{18}O$ are displayed in (a)
and (d), δD in (b) and (e) and changes in d-excess in (c) and (f), plotted against the average temperature during the experiments. The
colour code in (a), (b) and (c) show the average initial snow isotopic composition. The colour code in (d), (e) and (f) shows the change in
specific humidity inside the wind tunnel due to the sublimation of snow until the sampling of the corresponding snow sample. The
warming (red cross) and cooling (black cross) experiments are excluded from the colour coding because of their extreme values that are
given in Table 1. Grey circled data points are the experiments conducted in January, in which the specific humidity increase was calculated
from the *Hygroclip* sensors in the absence of the CRDS measurements. The marker size indicates the total transport duration in the range
of 49 min to 180 min with bigger markers representing longer transport times. Error bars account for the total error calculated from the
standard error of the initial mean and the measurement uncertainty of the individual airborne snow sample.

The snow samples taken from the accumulated snow show a clear difference between the samples from the inner part and the
surface layer of the accumulated snow. All 16 snow samples from the May period taken from the inner part of the snow
accumulation have an isotopic composition closer to the initial snow compared to the samples from the surface layer of the
accumulated snow. In 6/16 experiments the inner accumulation samples had the same (±uncertainty) isotopic composition
for all three isotope variables as the initial snow.

3.2.2 The co-evolution of atmospheric and snow variables

Atmospheric variables

The changes we observe in the PPP and the isotopic composition of the airborne snow are a result of the interplay between
the snow particles and the atmospheric conditions in the wind tunnel. For each experiment, the atmospheric conditions were
closely monitored. In the following, we summarise the evolution pattern of all experiments and show the data of experiment
No. 9 as a representative example in Fig. 4.

At the start of the experiments, when the conditions inside the wind tunnel were stable, the wind generation was initiated (Fig. 4(d)), and shortly after the snow was added to the wind tunnel (Fig. 4, purple shading). Immediately after the snow introduction started, the RH_{ice} increased sharply and reached saturation with respect to ice within minutes (Fig. 4(a)). With the start of the wind generator system, the air temperature inside the wind tunnel started to increase as heat was generated by the propellor motor (Fig. 4(c), red line). This wind tunnel heating was modulated by the laboratory's cooling system in a way that the cooling phases of the laboratory climate system also slowed down the temperature increase inside the wind tunnel (Fig. 4(c), yellow line). The total temperature change for each experiment is given in Table 1. Concurrently with the temperature, the specific humidity inside the wind tunnel evolves as the air is at (close-to) saturation conditions, hence the saturation vapour pressure defines the humidity level (Fig. 4(b)). This general evolution of the meteorological variables with the temperature evolution dominating the (saturation) humidity level inside the wind tunnel was observed for all experiments except the warming experiment in which the air only briefly reaches saturation after ~1 h due to continuous strong heating of the wind tunnel air stream. The sampling events every 15–30 min can be identified as short-lived dips of 1–2 min in the wind speed (Fig. 4(d)).

Vapour

The evolution of the isotopic composition of the vapour (Fig. 4 (e), (g), (i)) during and after the snow introduction cannot be generalised but categorised into the following:

During the snow introduction, most of the 16 experiments in May 2023 showed a strong enrichment in the vapour phase of $\delta^{18}O$ (>0.5 ‰, 13/16), δD (>4 ‰, 16/16) and an increase in d-excess (>3 ‰, 6/16). The remaining experiments showed no prominent change during snow introduction in vapour $|\Delta\delta^{18}O|$ (<0.5 ‰, 3/16) whereas for d-excess 4/16 experiments showed only a minimal increase (<3 ‰) and 6/16 experiments showed a slight decrease (>-3 ‰) in the vapour signal. The subsequent evolution in the 14 constant temperature experiments can be categorized into:

i)   continued increase in $\delta^{18}O$ (2/14), δD (6/14) and d-excess (8/14)

ii)   reversed evolution, i.e. strong ($|\Delta\delta^{18}O| > 0.5$ ‰) depletion in $\delta^{18}O$ (3/14)

iii)   (almost) constant values in $|\Delta\delta^{18}O|$ (<0.5 ‰, 8/14), $|\Delta\delta D|$ (<4 ‰, 6/14) and $|\Delta d\text{-excess}|$ (<3 ‰, 6/14)

iv)   varying evolution in $\delta^{18}O$ (1/14) and δD (2/14)

In the warming experiment, $\delta^{18}O$, δD and d-excess all showed a pronounced increase after the snow introduction had ended until the end of the experiment. Finally, the cooling experiment showed a variable isotopic evolution with a sequence of pronounced phases of depletion, enrichment, and another depletion phase in both $\delta^{18}O$ and δD, whereas the d-excess stayed constant ($|\Delta d\text{-excess}|$ <3 ‰) during the entire experiment.
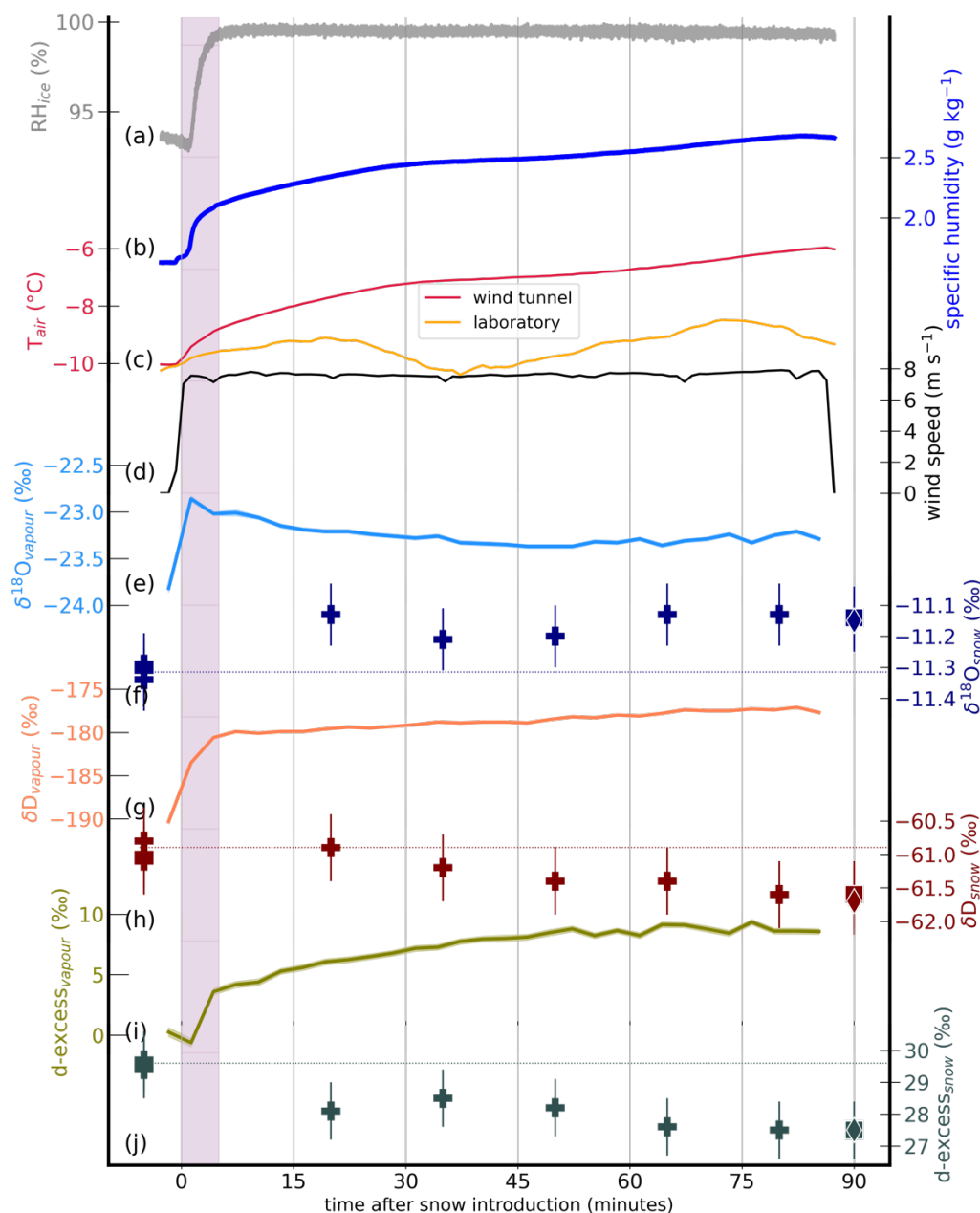
Fig. 4: The time evolution of all monitored variables in the exemplary experiment No. 9 The meteorological variables inside the wind tunnel are shown in panels: (a) relative humidity with respect to ice, (b) CRDS specific humidity readings, (c) wind tunnel and laboratory temperature, (d) wind speed. The period of snow introduction is shaded in purple. After the snow introduction, the wind tunnel was closed and only opened for brief periods of 1–2 min during airborne snow sampling which are visible as dips in the wind measurements. The evolution of the 3-min averaged water vapour isotopic composition is shown with standard error of the mean uncertainty shading for $\delta^{18}O$ in (e), δD in (g) and d-excess in (i). The isotopic composition of the snow samples is given in (f) for $\delta^{18}O$, in (h) for δD, and in (j) for d-excess with the measurement uncertainty as error bars. The snow samples taken from the accumulated snow are shown as square (surface layer/acc_out) and diamond (inside of accumulation/acc_in) markers. The horizontal lines indicate the initial isotopic composition (mean of three samples).

4   Discussion

4.1 Airborne snow metamorphism

SSA

All experiments with µCT measurements show a rapidly decreasing SSA with transport time that can be described by the
425   typical exponential decay function (Cabanes et al., 2003). This phenomenon is well known inside the snowpack where the
SSA decreases over time in isothermal and under temperature gradient conditions due to snow metamorphism (Harris Stuart
et al., 2023; Schleef et al., 2014b) but seems to happen at an increased rate of 1–2 orders of magnitude during airborne
transport. The decrease in SSA describes a change in the particle morphology and the rapidness with which the SSA
decreases suggests a rounding and growing of particles through abrasion or metamorphic mechanisms since large spheres
430   have the lowest SSA values (Legagneux et al., 2002). These results are in line with the changes observed in the sphere size
distribution analysis that are discussed below. Note here, that simple mechanic fragmentation of snow particles does
conceptually not lead to a significant change in sample SSA and can thus not explain the decrease in SSA. The initial SSA
values of the experiments vary slightly, which is due to the storage time between snow production and experiment start
(Table 1). Although the snow was stored at -20 °C to slow down snow metamorphism prior to the experiment start, the older
435   the snow was when introduced into the wind tunnel, the lower the initial SSA. We find no direct dependency of SSA decay
rate on temperature which is in line with wind tunnel experiments studying the metamorphism rate of accumulated snow
under wind influence for temperatures < -5 °C (Walter et al., 2023) but different from snowpack metamorphism under no-
wind conditions (Harris Stuart et al., 2023; Schleef et al., 2014b). As the driving processes for snow metamorphism are
sublimation and vapour deposition, it seems plausible that slight spatial variability in the saturation conditions (super-
440   saturation, saturation, or sub-saturation) in the wind tunnel mask the generally expected positive temperature dependency
with higher SSA decay rates for isothermal snowpack metamorphism.

Particle size and shape

The evolution of the fitted sphere size distribution with transport time shows a general broadening and increase in skewness
with a shift of the dominant sphere size to larger diameters. As the algorithm finds the maximum sphere size it can fit at any
445   given location inside the ice matrix of the sample (Hildebrand and Rüegsegger, 1997), this can be interpreted as larger
particles emerging and a rounding of the individual particles with transport time. These observations are somewhat
surprising since aeolian transport of snow is associated with fragmentation and abrasion of particles, and thus a decrease in
particle sizes as snow crystals break apart due to mechanical stresses (Comola et al., 2017; Sato et al., 2008). Notably, the
evolution of sphere size distribution resembles the evolution observed during isothermal metamorphism (Legagneux and
450   Domine, 2005; Flin et al., 2004). We note here that care must be taken when interpreting fitted sphere sizes as particle sizes
(Löwe et al., 2011) and mention the difficulty in the assessment of particle "size" in snow in general (Fierz et al., 2009). In
fact, our observations of growing sphere sizes do not contradict the initial snow particle fragmentation mechanism through
impact, as pure fragmentation does not significantly influence fitted sphere size distributions within a snow sample. On the

other hand, abrasion producing very fine snow dust could increase the occurrence of very small, fitted sphere sizes.
However, we see a disappearance of the smallest fitted sphere sizes and an appearance and increase of bigger sphere sizes of
>100 μm. One mechanical mechanism that could explain the shift to larger sphere sizes could be the collision and
subsequent aggregation of snow particles as known from ice cloud observations (Pruppacher and Klett, 1997). In ice clouds,
this process of coalescing snow particles is an important ingredient in the growth of ice crystals and the formation of snow
aggregates (Lo and Passarelli, 1982; Mitchell, 1988). Another plausible mechanism for the growing of particles is airborne
snow metamorphism with continuous sublimation from and vapour deposition on the suspended particles (Walter et al.,
2023). The (close-to-) saturation conditions inside the wind tunnel a few minutes subsequent to the snow introduction are
favourable conditions for this chain of thermodynamic processes. The growing and rounding of the particles may thus be
explained by airborne metamorphic growth with vapour being preferentially sublimated from convex sub-grain boundaries
and preferentially deposited in concavities in analogy to isothermal metamorphism in a snowpack (Wakai et al., 2005;
Colbeck, 2001, 1998). Vapour deposition on suspended snow particles has been previously modelled in large eddy
simulations (LES) of wind-blown snow (Sigmund et al., submitted; Sharma et al., 2018) but could not be validated against
observations so far. As was shown by Sharma et al. (2018) these deposition-enabling conditions can exist even under slightly
under-saturated surrounding conditions (usually generally favouring sublimation) if the particle temperature is lower than the
surrounding air temperature. Traditionally, a temperature equilibrium between the particle and surrounding air is assumed
following the well-established and frequently used sublimation rate estimation by Thorpe and Mason (1966). This
assumption does not allow for the deposition of vapour on the suspended particle. However, as the temperature in the wind
tunnel was not constant, it is possible that the particle temperature was lagging the air temperature preventing the
establishment of a temperature equilibrium between the air and the snow particle. The accumulated snow on the ground and
the walls of the wind tunnel could further act as a cooling source in the wind tunnel system that could especially cool
saltation particles. Sharma et al. (2018) found a direct dependency between particle diameter and lag time. This would
suggest that while small particle fragments (from e.g. abrasion) might equilibrate faster and consequently sublimate entirely,
bigger and colder particles might attract vapour deposition and thus trigger a positive feedback. Indeed, we find that the
smallest sphere sizes detected initially disappear with time which can be interpreted as the full sublimation of the smallest
particle fragments. These explanations combined can resolve the apparently conflicting observations of growing particles
due to vapour deposition while we see a net humidity increase from snow sublimation throughout the experiments.

4.2 The isotopic signature of airborne snow metamorphism (explained)

We have observed changes in the isotopic composition of vapour and notably also in the snow during the experiments. The
changes in the snow isotopic composition support the theory of airborne snow metamorphism as driver for PPP changes
since involved phase changes lead to changes in the isotope signals. Mechanical mechanisms such as abrasion, clustering,
and aggregation of particles, however, would not lead to changes in the bulk isotopic composition of the snow sample.

Investigating the amplitude and sign of the changes in the snow isotopic signal allows further deduction about the processes at play.

Sublimation-controlled metamorphism immediately after snow introduction and during warming experiment

The near-universal signal of enrichment in snow δ^{18}O and δD while d-excess decreases in the first airborne snow sample
490   suggests sublimation-dominated metamorphic mechanisms affecting the snow and its PPP during and immediately after snow introduction. This is in line with the steep humidity and RH increase to (close-to) saturation conditions in this period. Similarly, the continuous positive trend in snow δ^{18}O and δD and negative trend in d-excess during the persistent sub-saturated conditions in the warming experiment suggests isotopic fractionation during net sublimation conditions. The existence of fractionation during sublimation has been controversially discussed as the slow process of self-diffusion in ice
495   usually does not allow mixing on time scales fast enough to incorporate the sublimation signal in the remaining solid matrix (Hu et al., 2022; Friedman et al., 1991). Thus, it was assumed that sublimation happens according to a layer-by-layer removal of the water molecules which would not alter the isotopic composition of the remaining ice. Following this reasoning, current isotope-enabled climate models do not account for fractionation during snow sublimation (Dütsch et al., 2023; Cauquoin and Werner, 2021; Moore et al., 2016; Pfahl et al., 2012). Ever-growing evidence, however, documents an
500   enrichment in δ^{18}O and δD in snow isotopic composition during and after sublimation of surface snow (Hughes et al., 2021; Sokratov and Golubev, 2009; Stichler et al., 2001) analogous to the results of $\Delta\delta^{18}$O and $\Delta\delta$D in the first airborne snow samples and the trend analysis in the warming experiment. The concurrent decrease of snow d-excess is also in agreement with previous laboratory studies that likewise found a decrease in d-excess under sublimation conditions (Hughes et al., 2021). It is an indicator of the existence of non-equilibrium, diffusive processes which aligns with the strong sublimation
505   signal in the humidity observations. Thus, the wind tunnel results presented in this study further add to previous studies with δ^{18}O and δD enrichment and d-excess decrease during sublimation-favourable conditions.

These sublimation-dominated conditions in the wind tunnel at the beginning of the experiments can explain the PPP changes observed in the first airborne samples. The shift in the smallest sphere sizes is largest between the initial snow and first airborne snow samples. Highly dendritic parts of the airborne particles either first get abraded and fragmented or sublimate
510   directly from the airborne dendritic particles which explains the disappearance of the smallest fitted sphere sizes and likewise, the decrease in SSA as particles start to round. Once (close-to-) saturation conditions are reached, the conditions shift towards deposition-controlled metamorphism.

Deposition-controlled metamorphism during aeolian transport

We hypothesize that the further decrease in SSA and the gradual shift towards bigger sphere sizes is due to vapour
515   deposition on the airborne particles that consequently grow with aeolian transport time. This hypothesis is supported by the observed maximum changes in snow isotopic composition that can be explained by assuming vapour deposition on suspended particles. Following this assumption, the vapour that gets deposited on the suspended particles controls the sign and magnitude of the change observed in the airborne snow samples. Indeed, the changes can be explained by analysing the isotopic composition of the solid that is formed (deposited) from vapour inside the wind tunnel and the initial snow that is

520   introduced. Figure 5 (b) shows this analysis for δD assuming equilibrium fractionation. The solid disequilibrium analysis (Sec. 1) shows that, generally, experiments in which the combination of water vapour and temperature inside the wind tunnel produce equilibrium deposit that is enriched compared to the initial snow (positive disequilibrium), show a positive change in δD. If, however, the formed equilibrium deposit is depleted compared to the initial snow (negative disequilibrium), the change in δD is negative. A linear fit to this data is significant (p=0.004) with R^2=0.46. It is worth mentioning that a

525   temperature uncertainty of +1 K can produce a fit with a zero origin. In Fig. 5 (a) the same analysis is shown for δ^{18}O. As δ^{18}O is more sensitive to non-equilibrium conditions than δD (Majoube, 1970; Merlivat and Nief, 1967), it is not surprising that the disequilibrium analysis of formed equilibrium deposits cannot explain the observations. Instead, the changes in δ^{18}O can be explained by allowing for a colder particle temperature compared to the surrounding air. As discussed earlier, this condition of a particle-air temperature gradient that leads to supersaturation with respect to the particle surface is a

530   requirement for the growth of particles through vapour deposition and the changes in δ^{18}O support this theory. Isotopic fractionation under supersaturation conditions can produce solid deposits with very depleted δ^{18}O values compared to pure equilibrium fractionation (Jouzel and Merlivat, 1984). The resulting δ^{18}O value of the deposit is dependent on the supersaturation condition (set by the particle-air temperature difference) that strongly influences the non-equilibrium fractionation of δ^{18}O. The changes in snow δ^{18}O during the wind tunnel experiments are thus dependent on the combination

535   of initial snow and vapour isotopic composition and the particle-air temperature difference that defines the supersaturation. Everything except the particle-air temperature difference is measured in the wind tunnel experiments, which allows to estimate the temperature difference needed to observe negative changes in snow δ^{18}O values. Following Jouzel and Merlivat (1984), we calculate the minimum supersaturation conditions necessary for negative changes in snow δ^{18}O. From this, we deduce the associated temperature difference between air and particle using saturation vapour pressure functions of Goff and

540   Gratch (1946) (see colour code in Fig. 5 (a)). As can be seen, the four experiments in which a negative change in snow δ^{18}O was observed during the experiments, are indeed cases in which reasonable temperature differences of 0.5–1.0 K are enough to result in the negative δ^{18}O changes that were observed. Generally, the calculated required temperature difference shows a strong correlation with maximum observed changes in snow δ^{18}O with R^2=0.47 and p=0.004 (not shown).

In summary, the observed changes in snow isotopic composition support the theory of growing particles due to vapour

545   deposition and the existence of the prerequisite of particles that are colder than the surrounding air.
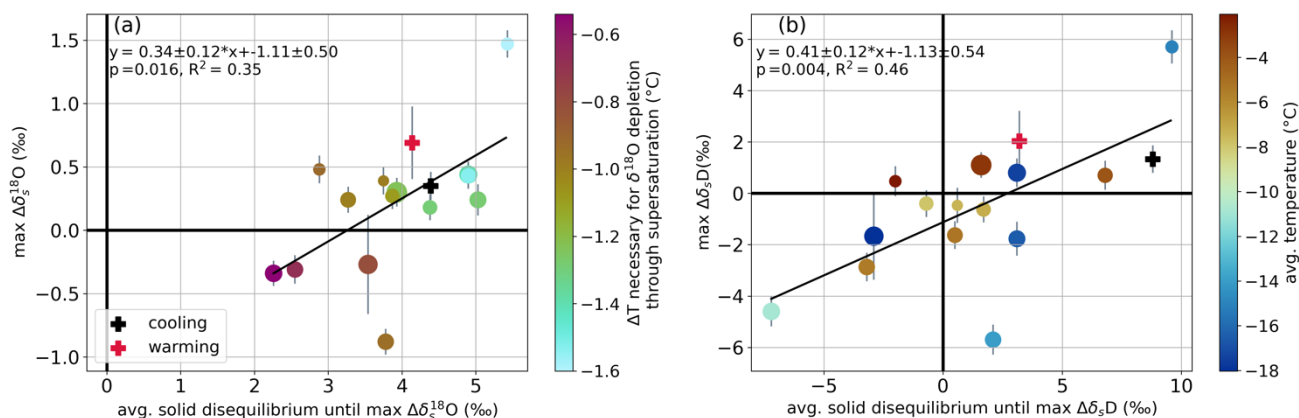
Fig. 5: Changes in snow isotope signal explained The y-axes show the maximum isotopic change observed between airborne snow sample and initial snow sample for $\delta^{18}O$ in (a) and for δD in (b) (same as Fig. 3 (d) and (e)). The x-axes show the average solid disequilibrium in the period after the snow had been added until the maximum change in snow isotopic composition was observed. The colour code in (b) shows the average temperature of the experiments. In (a) the colour code shows the minimum particle-air temperature difference required to produce supersaturation conditions that lead to a negative $\delta^{18}O$ change in the snow. Linear least-square fits to the data and the corresponding fitting statistics are given.

4.2.1 Fractionation during sublimation?

As outlined above, this study finds isotopic enrichment in the first airborne snow samples under net sublimation conditions supporting previous snow-focused studies that present evidence for fractionating sublimation (Hughes et al., 2021; Sokratov and Golubev, 2009; Stichler et al., 2001). A recent study by Wahl et al. (2021) further substantiated the existence of isotopic fractionation during net sublimation from a snow surface by measuring the isotopic composition of the near-surface sublimation flux which showed to be significantly depleted compared to the surface snow isotopic composition. Besides the change in the snow isotope signal, the wind tunnel data provides additional supporting evidence through the vapour isotope signal. That is the changes observed in the vapour isotopic composition during snow introduction are better described by assuming a mixing between already present and newly produced water vapour originating from fractionating sublimation rather than from non-fractionating sublimation. In other words, the initial disequilibrium prior to snow introduction (i.e. vapour produced by fractionating sublimation) is a better predictor for the changes in vapour isotopic composition during the snow introduction ($R^2(\delta^{18}O)$ = 0.76, $R^2(\delta D)$ = 0.68) than the mere difference in vapour and snow isotopic composition (i.e. vapour produced by non-fractionating sublimation) ($R^2(\delta^{18}O)$ = 0.47, $R^2(\delta D)$ = 0.28). For corresponding plots see SM Fig. S3. However, we want to point out that our observations of an isotopic deposition signal during general net sublimation (specific humidity increase) suggests an alternative explanation for the observed fractionation during net sublimation. Snow metamorphism happens on the micro-scale driven by net vapour-pressure gradients where "*metamorphic sublimation*" and "*metamorphic deposition*" can co-exist within the snowpack, while being spatially separated on the micro-scale, e.g. within one snow crystal. This process is happening continuously in the snowpack (Colbeck, 1982), and evidently also during airborne transport with periods of varying dominance of one process over the other. This concept of airborne snow

metamorphism is schematically visualised in Fig. 6. Thus, observations of isotopic fractionation during net sublimation do
575 not require that *metamorphic sublimation* is indeed fractionating if simultaneous *metamorphic deposition* is. The isotopic
enrichment in the solid matrix could thus stem from enriched deposit rather than a surface becoming enriched by
sublimation. As in our experiment, this would require that the deposit has a lower d-excess than the snow particle, on which
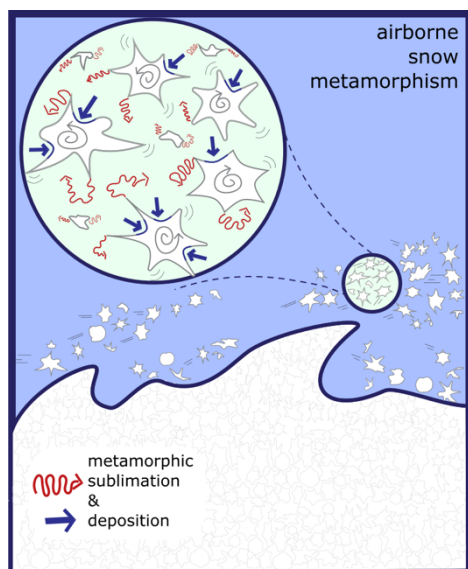
it gets deposited, leading to a d-excess decrease, rather than the theoretical d-excess increase during vapour deposition (Casado et al., 2016). Ultimately, both d-excess increase and decrease in a snowpack can be associated with metamorphic deposition depending on the disequilibrium between snow and vapour. The macro-scale humidity gradient, e.g. the gradient between the snow surface and the near-surface atmosphere, defines the direction of the net humidity flux but isotopic fractionation is defined through the micro-scale metamorphic processes. These considerations are needed to find a physically sound explanation for the evidently fractionating net sublimation. Clearly, for realistic isotope-enabled climate model simulations an implementation of a bulk fractionation factor for net surface sublimation is needed.

Fig. 6 Conceptual scheme of airborne snow metamorphism The scheme visualises that micro-scale processes of *metamorphic sublimation* and *metamorphic deposition* are happening continuously and simultaneously even under net sublimation conditions. We hypothesize that metamorphic vapour deposition on the largest airborne particles due to temperature differences between surrounding air and particle surface together with preferential sublimation of convex sub-grain boundaries and preferential deposition in concavities cause
595 a decrease in SSA and particle growth.

4.3 Field application and experimental limitations

Airborne snow metamorphism as observed in the ring wind tunnel experiments is expected to be dominant in the saltation
layer of wind-blown snow. The (close-to-) saturation conditions inside the ring wind tunnel better resemble saltation layer
than suspension layer conditions on average, but Sigmund et al. (2021) have shown that downward moisture fluxes can also
600 occur in suspension clouds. Saturated saltation layers (<1 m height) have been frequently observed in coastal Antarctic areas
whereas saturation in the blowing snow cloud of heights >5 m requires very high wind speeds and high particle
concentrations (Amory and Kittel, 2019). A deepening of the saturated layer is favoured in stable atmospheric boundary
layers with strong near-surface temperature gradients (Mann et al., 2000). Thus, we expect airborne snow metamorphism to
reach larger heights during stable boundary layers which are frequently observed during polar night conditions. Additionally,
605 the particle-air temperature gradient needed to facilitate vapour deposition and particle growth is predominantly found in the
saltation layer, whereas the thermal equilibrium assumption seems to adequately describe the conditions in the suspension
layer (Sharma et al., 2018). Indeed, the particle-air temperature difference simulated in LES close to the cold snow surface is
of comparable magnitude (~0.5 K, Sigmund et al., (submitted)) to the results obtained from the δ^{18}O isotope analyses. The

sustained deposition conditions in our experiments might also be favoured by the continued warming of the wind tunnel air
610   with the particle temperatures lagging. The motor heating is an experimental limitation that hinders the direct analogy to
real-world conditions where the energy balance inside a blowing snow cloud is largely defined by the sublimation process
itself with sublimation leading to a cooling which essentially self-inhibits ongoing sublimation (Sigmund et al., 2021; Amory
and Kittel, 2019). An additional experimental limitation is the interaction of airborne particles with the physical boundaries
of the wind tunnel, i.e. the walls and floor which results in additional collision impact compared to nature or straight wind
615   tunnels. Furthermore, the flow field inside the wind tunnel does not fully develop into a logarithmic boundary layer flow and
centrifugal forces act on the particles in the curved section (Sommer et al., 2017). However, as Walter et al. (2023) outlines
for the same wind tunnel, the individual particle transport characteristics of impact angle and velocities, both at the wind
tunnel walls and snow surface, are comparable to particle transport characteristics in the saltation layer of a fully developed
boundary flow. In summary, the sheer setup of the wind tunnel construct prevents an unequivocal comparison to real-world
620   conditions. Yet, the experiments have provided a means to discover a physical process that is not discernible from fixed-
location in-situ measurements of wind-blown snow without knowledge of provenance and prior evolution of observed
airborne particles. We point out that the absolute values of available field observations of particle shape and size
distributions do not conflict with the findings of this study but might have implicitly entailed airborne snow metamorphism
markings.   The   largest   particles   that   are   observed   in   the   experiments   contain   sphere   sizes   of
625   200–300 μm. These sphere sizes are well within in-situ observed particle size distributions (Nishimura et al., 2014;
Nishimura and Nemoto, 2005) and significantly smaller than fresh snow particles (Comola et al., 2017; Sato et al., 2008)
therefore not contradicting snowflake fragmentation. Interestingly the most abundant sphere sizes in the last airborne snow
samples have diameters of 60–70 μm which would be considered small particle sizes in wind-blown particle size
distributions. However, care must be taken when comparing particle size estimates from snow particle counter (Nemoto and
630   Nishumura, 2001) and sphere fitting routines (Hildebrand and Rüegsegger, 1997). Which metric is superior depends on the
application and question that is being addressed. Highly dendritic fresh snowflakes can be large concerning the particle size
but have very high SSA values which is better represented through the small sphere size metric.

4.4 Implications of airborne snow metamorphism

4.4.1 Influence on snow surface and snowpack characteristics

635   The wind tunnel experiments have shown that airborne particles can grow thermodynamically under certain conditions. This
process is not accounted for in wind-blown snow models (Melo et al., 2022) nor is it accounted for in calculations of mass
removal by snow sublimation during blowing snow events (Palm et al., 2017). Unfortunately, we have no means to estimate
the mass of redeposited vapour in our experiments. Estimates about the impact on mass balance and sublimation flux
calculations are beyond the scope of this study. Yet, the changes in airborne PPP can be set in the context of known changes
640   in snowpack characteristics under wind influence.

Wind has been shown to increase the density of snow (Walter et al., 2023; Liston et al., 2007; Lehning et al., 2002). Crucial for this is the presence of wind-transported snow (Sommer et al., 2017). The surface snow density increase is associated with grain settling and packing which is more efficient for smaller and rounder particles (The Firn Symposium team et al., 2024; Parteli et al., 2014). The combination of mechanical abrasion and fragmentation (Comola et al., 2017) together with

645   metamorphic rounding could thus increase the densification rate under wind influence. Likewise, SSA has been shown to decrease under wind influence (Walter et al., 2023; Legagneux et al., 2002). We suggest that this observed wind-SSA relationship is largely due to airborne snow metamorphism. These modifications of SSA affect the radiative characteristics of the resulting snowpack with SSA decay leading to a reduction in snow albedo (Flanner and Zender, 2006). Consequentially, airborne snow metamorphism could reduce the albedo of the ultimately accumulated snow.

650   **4.4.2 The isotopic signature of wind-blown snow**

Snowpack metamorphism has been shown to influence the isotopic composition of snow in polar areas depending on the temperature gradient in the snowpack (Harris Stuart et al., 2023; Casado et al., 2021). Laboratory experiments have further shed light on the interplay between snow and vapour isotopic composition during snow metamorphism (Ebner et al., 2017). Similarly, the isotopic signature of the wind-blown snow event in the wind tunnel was dependent on the combination of

655   vapour and snow isotopic composition and the resulting disequilibrium. Thus, it is not possible to unambiguously predict the expected changes in the snow isotope signal under wind influence without considering water vapour isotope variability which is driven by synoptic-scale atmospheric variability (Aemisegger et al., 2022; Bagheri Dastgerdi et al., 2021). However, the results suggest that a strong d-excess decrease can be linked to airborne metamorphism. Thus, it could be possible to use the snow isotopic composition to differentiate between wind-blown snow and precipitated snow. Further field

660   studies need to support this idea.

Another interesting implication of the wind tunnel findings is the interpretation of the snow isotopic composition as a climate signal. Stable water isotope records obtained from ice cores in the polar areas are valuable climate proxy records that allow the reconstruction of paleoclimate and ice sheet dynamics in these remote areas (Stenni et al., 2017; Vinther et al., 2009; Jouzel et al., 2007). The foundation for these paleoclimate interpretations of isotope records is the observation of a linear

665   relationship between annual mean temperatures and corresponding average precipitation isotopic composition (Dansgaard, 1964). However, in low accumulation, dry regions of the ice sheets, where the oldest ice cores are obtained from, evidence accumulates for the influence of post-depositional processes on the snow isotopic composition, and thus on the climate signal that is stored in the snow (Town et al., 2024; Dietrich et al., 2023; Zuhr et al., 2023a; Wahl et al., 2022). This study shows that wind transport is one more post-depositional process that has the potential to add a local climate signal to the

670   snow isotopic composition. The magnitude of observed snow isotopic change in the experiments due to airborne snow metamorphism is within the range of observed daily snow surface isotope variability on clear-sky and calm days (Zuhr et al., 2023b; Wahl et al., 2022), yet evolving within 1–2 h. Thus, modeling studies will be needed to estimate the impact of the combined post-depositional processes on the original precipitation isotopic composition that is also proclaimed to carry

information about the moisture source conditions (Uemura et al., 2012; Aemisegger et al., 2022). Our results suggest that
675   locations with frequent strong winds might show strong potential for an overprinting of the original d-excess source region
signal and support the interpretation of studies with measured low d-excess values (Hu et al., 2022).

5   Conclusions

We used ring wind tunnel experiments to study the governing micro-scale processes of aeolian snow transport that are
difficult to observe in the field. MicroCT measurements of airborne snow samples documented a growing and rounding of
680   suspended particles and a consequential decrease in SSA with transport time. Stable water isotope analysis of airborne snow
and water vapour suggests airborne snow metamorphism rather than mechanical mechanisms as a driver for the observed
particle evolution. Snow sublimation dominated the metamorphic process during sub-saturation conditions, while vapour
deposition dominated in (close-to) saturated conditions comparable to saltation layer conditions during wind-blown snow
events. Supporting previous modeling studies, the wind tunnel results further indicated a particle-air temperature difference,
685   particularly for larger particles that favour the deposition of vapour and thus particle growth while smaller particles get
sublimated entirely. This process of airborne snow metamorphism is difficult to observe in-situ with point measurements of
wind-blown snow, where the origin and preceding history of the airborne particles is unknown. Thus, it is a hitherto
unobserved process, yet our conclusions do not contradict available in-situ measurements of airborne particle distributions
during blowing snow events. Instead, our findings refine the process understanding of wind-blown snow with possible
690   implications for mass and energy balance and moisture budget calculations during blowing and drifting snow events.
In this study, the isotopic fingerprint of airborne snow metamorphism was used to pinpoint its existence. As the isotopic
signature of airborne snow metamorphism partly overprints the original snow isotopic signal it offers the potential to act as
tracer for aeolian snow transport. Furthermore, it questions the conservation of moisture source region signals in the snow
isotopic composition in windy areas with frequent wind-blown snow events. Future field-based studies will be valuable to
695   support our laboratory-based observations of a link between airborne snow transport, particle physical properties and stable
water isotopes.

700

Data availability statement

705   The data collected during the wind tunnel experiments and presented in this paper are available in Wahl et al. (2024).

Author contribution

Funding for this work was acquired by ML. FA and ML provided resources. SW conceptualized and designed the experiments with inputs from FA, ML and BW. The data was curated by SW and BW with help from LB. Data calibration was performed by SW. The data was analysed by SW with feedback from FA, BW and ML. SW did visualisations and
710   writing of the original draft and all authors edited the manuscript.

Competing interests

The authors declare that they have no conflict of interest.

Acknowledgements

This work was funded by grant 179130 from the Swiss National Science Foundation. We thank the ETH atmospheric
715   dynamics group (Prof. Heini Wernli) for providing liquid water standards, a pump and nylon filters. We thank Dr. Katrin Meusburger from WSL for providing the SDM, and Dr. Julia Schmale from EPFL for lending us the MFC. We greatly appreciated the speed and flexibility of the sample analyses performed by the isotope laboratory at both the University of Freiburg, Germany and the Paul Scherrer Institute, Switzerland. We also thank all users of the SLF cold-laboratory facilities for sharing the cold-laboratory space and especially Matthias Jaggi and Benjamin Eggert for reliable and prompt support and
720   help with the wind tunnel experiments. We thank Dr. Armin Sigmund for helpful discussions on particle-air interactions.

References

Aemisegger, F., Sturm, P., Graf, P., Sodemann, H., Pfahl, S., Knohl, A., and Wernli, H.: Measuring variations of δ18O and δ2H in atmospheric water vapour using two commercial laser-based spectrometers: An instrument characterisation study, Atmospheric Measurement Techniques, 5, 1491–1511, https://doi.org/10.5194/amt-5-1491-2012, 2012.

725   Aemisegger, F., Spiegel, J. K., Pfahl, S., Sodemann, H., Eugster, W., and Wernli, H.: Isotope meteorology of cold front passages: A case study combining observations and modeling, Geophysical Research Letters, 42, 5652–5660, https://doi.org/10.1002/2015GL063988, 2015.

Aemisegger, F., Trachsel, J., Sadowski, Y., Eichler, A., Lehning, M., Avak, S., and Schneebeli, M.: Fingerprints of Frontal Passages and Post-Depositional Effects in the Stable Water Isotope Signal of Seasonal Alpine Snow, JGR Atmospheres, 127,
730   e2022JD037469, https://doi.org/10.1029/2022JD037469, 2022.

Amory, C. and Kittel, C.: Brief communication: Rare ambient saturation during drifting snow occurrences in coastal East Antarctica, The Cryosphere, 13, 3405–3412, https://doi.org/10.5194/tc-13-3405-2019, 2019.

Amory, C., Naaim-Bouvet, F., Gallée, H., and Vignon, E.: Brief communication: Two well-marked cases of aerodynamic adjustment of sastrugi, The Cryosphere, 10, 743–750, https://doi.org/10.5194/tc-10-743-2016, 2016.

735 Avak, S. E., Trachsel, J. C., Edebeli, J., Brütsch, S., Bartels-Rausch, T., Schneebeli, M., Schwikowski, M., and Eichler, A.: Melt-Induced Fractionation of Major Ions and Trace Elements in an Alpine Snowpack, J. Geophys. Res. Earth Surf., 124, 1647–1657, https://doi.org/10.1029/2019JF005026, 2019.

Bagheri Dastgerdi, S., Behrens, M., Bonne, J.-L., Hörhold, M., Lohmann, G., Schlosser, E., and Werner, M.: Continuous monitoring of surface water vapour isotopic compositions at Neumayer Station III, East Antarctica, The Cryosphere, 15, 740 4745–4767, https://doi.org/10.5194/tc-15-4745-2021, 2021.

Bagnold, R. A.: The Physics of Blown Sand and Desert Dunes, Springer Dordrecht, 1941.

Bailey, A., Aemisegger, F., Villiger, L., Los, S. A., Reverdin, G., Quiñones Meléndez, E., Acquistapace, C., Baranowski, D. B., Böck, T., Bony, S., Bordsdorff, T., Coffman, D., De Szoeke, S. P., Diekmann, C. J., Dütsch, M., Ertl, B., Galewsky, J., Henze, D., Makuch, P., Noone, D., Quinn, P. K., Rösch, M., Schneider, A., Schneider, M., Speich, S., Stevens, B., and 745 Thompson, E. J.: Isotopic measurements in water vapor, precipitation, and seawater during EUREC [4] A, Earth Syst. Sci. Data, 15, 465–495, https://doi.org/10.5194/essd-15-465-2023, 2023.

Budd, W. F.: The drifting of nonuniform snow particles, National Academies Press, https://doi.org/10.17226/21297., 1966.

Cabanes, A., Legagneux, L., and Dominé, F.: Rate of Evolution of the Specific Surface Area of Surface Snow Layers, Environ. Sci. Technol., 37, 661–666, https://doi.org/10.1021/es025880r, 2003.

750 Casado, M., Cauquoin, A., Landais, A., Israel, D., Orsi, A., Pangui, E., Landsberg, J., Kerstel, E., Prie, F., and Doussin, J. F.: Experimental determination and theoretical framework of kinetic fractionation at the water vapour-ice interface at low temperature, Geochimica et Cosmochimica Acta, 174, 54–69, https://doi.org/10.1016/j.gca.2015.11.009, 2016.

Casado, M., Landais, A., Picard, G., Arnaud, L., Dreossi, G., Stenni, B., and Prié, F.: Water Isotopic Signature of Surface Snow Metamorphism in Antarctica, Geophysical Research Letters, 48, 1–11, https://doi.org/10.1029/2021gl093382, 2021.

755 Cauquoin, A. and Werner, M.: High-Resolution Nudged Isotope Modeling With ECHAM6-Wiso: Impacts of Updated Model Physics and ERA5 Reanalysis Data, Journal of Advances in Modeling Earth Systems, 13, 1–19, https://doi.org/10.1029/2021MS002532, 2021.

Clifton, A., Rüedi, J.-D., and Lehning, M.: Snow saltation threshold measurements in a drifting-snow wind tunnel, J. Glaciol., 52, 585–596, https://doi.org/10.3189/172756506781828430, 2006.

760 Colbeck, S. C.: An overview of seasonal snow metamorphism, Reviews of Geophysics, 20, 45–61, https://doi.org/10.1029/RG020i001p00045, 1982.

Colbeck, S. C.: Sintering in a dry snow cover, Journal of Applied Physics, 84, 4585–4589, https://doi.org/10.1063/1.368684, 1998.

Colbeck, S. C.: Sintering of unequal grains, Journal of Applied Physics, 89, 4612–4618, https://doi.org/10.1063/1.1356427, 765 2001.

Comola, F., Kok, J. F., Gaume, J., Paterna, E., and Lehning, M.: Fragmentation of wind-blown snow crystals: BLOWING SNOW FRAGMENTATION, Geophys. Res. Lett., 44, 4195–4203, https://doi.org/10.1002/2017GL073039, 2017.

Craig, H.: Isotopic Variations in Meteoric Waters, Science, 133, 1702–1703, https://doi.org/10.1126/science.133.3465.1702, 1961a.

770 Craig, H.: Standard for Reporting Concentrations of Deuterium and Oxygen-18 in Natural Waters, Science, 133, 1833–1834, https://doi.org/10.1126/science.133.3467.1833, 1961b.

Dansgaard, W.: Stable isotopes in precipitation, Tellus, 16, 436–468, https://doi.org/10.3402/tellusa.v16i4.8993, 1964.

Dietrich, L., Steen-Larsen, H. C., Wahl, S., Faber, A.-K., and Fettweis, X.: On the importance of the humidity flux for the surface mass balance in the accumulation zone of the Greenland Ice Sheet, Ice sheets/Mass Balance Obs, 775 https://doi.org/10.5194/tc-2022-260, 2023.

Domine, F., Salvatori, R., Legagneux, L., Salzano, R., Fily, M., and Casacchia, R.: Correlation between the specific surface area and the short wave infrared (SWIR) reflectance of snow, Cold Regions Science and Technology, 46, 60–68, https://doi.org/10.1016/j.coldregions.2006.06.002, 2006.

Dütsch, M., Pfahl, S., and Sodemann, H.: The Impact of Nonequilibrium and Equilibrium Fractionation on Two Different 780 Deuterium Excess Definitions, Journal of Geophysical Research: Atmospheres, 122, https://doi.org/10.1002/2017JD027085, 2017.

Dütsch, M., Steig, E. J., Blossey, P. N., and Pauling, A. G.: Response of Water Isotopes in Precipitation to a Collapse of the West Antarctic Ice Sheet in High-Resolution Simulations with the Weather Research and Forecasting Model, Journal of Climate, 36, 5417–5430, https://doi.org/10.1175/JCLI-D-22-0647.1, 2023.

785 Ebner, P. P., Steen-Larsen, H. C., Stenni, B., Schneebeli, M., and Steinfeld, A.: Experimental observation of transient $\delta 18O$ interaction between snow and advective airflow under various temperature gradient conditions, The Cryosphere, 11, 1733–1743, https://doi.org/10.5194/tc-11-1733-2017, 2017.

Fierz, C., Armstrong, R. L., Durand, Y., Etchevers, P., Greene, E., McClung, D. M., Nishimura, K., Satyawali, P. K., and Sokratov, S. A.: The International Classification for Seasonal Snow on the Ground., in: IHP-VII Technical Documents in 790 Hydrology N°83, UNESCO-IHP, Paris, 2009.

Filhol, S. and Sturm, M.: Snow bedforms: A review, new data, and a formation model, Journal of Geophysical Research: Earth Surface, 120, 1645–1669, https://doi.org/10.1002/2015JF003529, 2015.

Flanner, M. G. and Zender, C. S.: Linking snowpack microphysics and albedo evolution, J. Geophys. Res., 111, 2005JD006834, https://doi.org/10.1029/2005JD006834, 2006.

795 Flin, F., Brzoska, J.-B., Lesaffre, B., Coléou, C., and Pieritz, R. A.: Three-dimensional geometric measurements of snow microstructural evolution under isothermal conditions, Ann. Glaciol., 38, 39–44, https://doi.org/10.3189/172756404781814942, 2004.

Friedman, I., Benson, C., and Gleason, J.: Isotopic changes during snow metamorphism, in: Stable Isotope Geochemistry: A Tribute to Samuel Epstein, vol. 3, edited by: Tayoir, H. P., O'Neill, J. R., and Kaplan, I. R., Geochemical Society, 211–221, 800 1991.

Gerber, F., Sharma, V., and Lehning, M.: CRYOWRF - a validation and the effect of blowing snow on the Antarctic SMB, Preprints, https://doi.org/10.22541/essoar.167591073.37929949/v1, 2023.

Goff, J. A. and Gratch, S.: Low-pressure properties of water from -160 to 212 °F, Transactions of the American Society of Heating and Ventilating Engineers, 95–122, 1946.

805   Gromke, C., Horender, S., Walter, B., and Lehning, M.: Snow particle characteristics in the saltation layer, J. Glaciol., 60, 431–439, https://doi.org/10.3189/2014JoG13J079, 2014.

Hagenmuller, P., Chambon, G., Lesaffre, B., Flin, F., and Naaim, M.: Energy-based binary segmentation of snow microtomographic images, J. Glaciol., 59, 859–873, https://doi.org/10.3189/2013JoG13J035, 2013.

Hagenmuller, P., Matzl, M., Chambon, G., and Schneebeli, M.: Sensitivity of snow density and specific surface area 810   measured by microtomography to different image processing algorithms, The Cryosphere, 10, 1039–1054, https://doi.org/10.5194/tc-10-1039-2016, 2016.

Harris Stuart, R., Faber, A.-K., Wahl, S., Hörhold, M., Kipfstuhl, S., Vasskog, K., Behrens, M., Zuhr, A. M., and Steen-Larsen, H. C.: Exploring the role of snow metamorphism on the isotopic composition of the surface snow at EastGRIP, The Cryosphere, 17, 1185–1204, https://doi.org/10.5194/tc-17-1185-2023, 2023.

815   He, S. and Ohara, N.: A New Formula for Estimating the Threshold Wind Speed for Snow Movement, J Adv Model Earth Syst, 9, 2514–2525, https://doi.org/10.1002/2017MS000982, 2017.

Heggli, M., Köchle, B., Matzl, M., Pinzer, B. R., Riche, F., Steiner, S., Steinfeld, D., and Schneebeli, M.: Measuring snow in 3-D using X-ray tomography: assessment of visualization techniques, Ann. Glaciol., 52, 231–236, https://doi.org/10.3189/172756411797252202, 2011.

820   Hildebrand, T. and Rüegsegger, P.: **A new method for the model-independent assessment of thickness in three-dimensional images**, Journal of Microscopy, 185, 67–75, https://doi.org/10.1046/j.1365-2818.1997.1340694.x, 1997.

Hori, M., Aoki, T., Tanikawa, T., Hachikubo, A., Sugiura, K., Kuchiki, K., and Niwano, M.: Modeling angular-dependent spectral emissivity of snow and ice in the thermal infrared atmospheric window, Applied Optics, 52, 7243–7255, https://doi.org/10.1364/AO.52.007243, 2013.

825   Hu, J., Yan, Y., Yeung, L. Y., and Dee, S. G.: Sublimation origin of negative deuterium excess observed in snow and ice samples from McMurdo Dry Valleys and Allan Hills Blue Ice Areas, East Antarctica, Journal of Geophysical Research: Atmospheres, https://doi.org/10.1029/2021jd035950, 2022.

Hughes, A. G., Wahl, S., Jones, T. R., Zuhr, A., Hörhold, M., White, J. W. C., and Steen-Larsen, H. C.: The role of sublimation as a driver of climate signals in the water isotope content of surface snow: Laboratory and field experimental 830   results, The Cryosphere, 15, 4949–4974, https://doi.org/10.5194/tc-15-4949-2021, 2021.

Jouzel, J. and Merlivat, L.: Deuterium and oxygen 18 in precipitation: Modeling of the isotopic effects during snow formation, Journal of Geophysical Research, 89, 11749, https://doi.org/10.1029/JD089iD07p11749, 1984.

Jouzel, J., Masson-Delmotte, V., Cattani, O., Dreyfus, G., Falourd, S., Hoffmann, G., Minster, B., Nouet, J., Barnola, J. M., Chappellaz, J., Fischer, H., Gallet, J. C., Johnsen, S., Leuenberger, M., Loulergue, L., Luethi, D., Oerter, H., Parrenin, F., 835   Raisbeck, G., Raynaud, D., Schilt, A., Schwander, J., Selmo, E., Souchez, R., Spahni, R., Stauffer, B., Steffensen, J. P., Stenni, B., Stocker, T. F., Tison, J. L., Werner, M., and Wolff, E. W.: Orbital and Millennial Antarctic Climate Variability over the Past 800,000 Years, Science, 317, 793–796, https://doi.org/10.1126/science.1141038, 2007.

Legagneux, L. and Domine, F.: A mean field model of the decrease of the specific surface area of dry snow during isothermal metamorphism, J. Geophys. Res., 110, 2004JF000181, https://doi.org/10.1029/2004JF000181, 2005.

840 Legagneux, L., Cabanes, A., and Dominé, F.: Measurement of the specific surface area of 176 snow samples using methane adsorption at 77 K, J. Geophys. ;Res., 107, https://doi.org/10.1029/2001JD001016, 2002.

Lehning, M., Bartelt, P., Brown, B., Fierz, C., and Satyawali, P.: A physical SNOWPACK model for the Swiss avalanche warning Part II. Snow microstructure, Cold Regions Science and Technology, 35, 147–167, 2002.

Liston, G. E., Haehnel, R. B., Sturm, M., Hiemstra, C. A., Berezovskaya, S., and Tabler, R. D.: Simulating complex snow 845 distributions in windy environments using SnowTran-3D, J. Glaciol., 53, 241–256, https://doi.org/10.3189/172756507782202865, 2007.

Lo, K. K. and Passarelli, R. E.: The Growth of Snow in Winter Storms:. An Airborne Observational Study, J. Atmos. Sci., 39, 697–706, https://doi.org/10.1175/1520-0469(1982)039<0697:TGOSIW>2.0.CO;2, 1982.

Löwe, H., Spiegel, J. K., and Schneebeli, M.: Interfacial and structural relaxations of snow under isothermal conditions, J. 850 Glaciol., 57, 499–510, https://doi.org/10.3189/002214311796905569, 2011.

Majoube, M.: Fractionation Factor of 18O between Water Vapour and Ice, Nature, 226, 1242–1242, https://doi.org/10.1038/2261242a0, 1970.

Mann, G. W., Anderson, P. S., and Mobbs, S. D.: Profile measurements of blowing snow at Halley, Antarctica, J. Geophys. Res., 105, 24491–24508, https://doi.org/10.1029/2000JD900247, 2000.

855 Melo, D. B., Sharma, V., Comola, F., Sigmund, A., and Lehning, M.: Modeling Snow Saltation: The Effect of Grain Size and Interparticle Cohesion, JGR Atmospheres, 127, https://doi.org/10.1029/2021JD035260, 2022.

Merlivat, L.: Molecular diffusivities of H216O, HD16O, and H218O in gases, The Journal of Chemical Physics, 69, 2864–2871, https://doi.org/10.1063/1.436884, 1978.

Merlivat, L. and Nief, G.: Fractionnement isotopique lors des changements d'etat solide-vapeur et liquide-vapeur de l'eau a 860 des temperatures inferieures a 0°C, Tellus, 1967.

Mitchell, D. L.: Evolution of Snow-Size Spectra in Cyclonic Storms. Part I: Snow Growth by Vapor Deposition and Aggregation, J. Atmos. Sci., 45, 3431–3451, https://doi.org/10.1175/1520-0469(1988)045<3431:EOSSSI>2.0.CO;2, 1988.

Mook, W. G.: Environmental isotopes in the hydrological cycle: principles and applications., International atomic energy agency and united Nations educational, scientific and cultural organization, Paris/Vienna, 2000.

865 Moore, M., Blossey, P. N., Muhlbauer, A., and Kuang, Z.: Microphysical controls on the isotopic composition of wintertime orographic precipitation, JGR Atmospheres, 121, 7235–7253, https://doi.org/10.1002/2015JD023763, 2016.

Murphy, D. M. and Koop, T.: Review of the vapour pressures of ice and supercooled water for atmospheric applications, Q. J. R. Meteorol. Soc., 131, 1539–1565, https://doi.org/10.1256/qj.04.94, 2005.

Nemoto, M. and Nishimura, K.: Numerical simulation of snow saltation and suspension in a turbulent boundary layer, J. 870 Geophys. Res., 109, 2004JD004657, https://doi.org/10.1029/2004JD004657, 2004.

Nemoto, M. and Nishumura, K.: Direct Measurement Of Shear Stress During Snow Saltation, Boundary-Layer Meteorology, 100, 149–170, https://doi.org/10.1023/A:1019267015986, 2001.

Nishimura, K. and Nemoto, M.: Blowing snow at Mizuho station, Antarctica, Phil. Trans. R. Soc. A., 363, 1647–1662, https://doi.org/10.1098/rsta.2005.1599, 2005.

875 Nishimura, K., Yokoyama, C., Ito, Y., Nemoto, M., Naaim-Bouvet, F., Bellot, H., and Fujita, K.: Snow particle speeds in drifting snow: Snow particle speeds in drifting snow, J. Geophys. Res. Atmos., 119, 9901–9913, https://doi.org/10.1002/2014JD021686, 2014.

Palm, S. P., Kayetha, V., Yang, Y., and Pauly, R.: Blowing snow sublimation and transport over Antarctica from 11 years of CALIPSO observations, The Cryosphere, 11, 2555–2569, https://doi.org/10.5194/tc-11-2555-2017, 2017.

880 Parteli, E. J. R., Schmidt, J., Blümel, C., Wirth, K.-E., Peukert, W., and Pöschel, T.: Attractive particle interaction forces and packing density of fine glass powders, Sci Rep, 4, 6227, https://doi.org/10.1038/srep06227, 2014.

Pfahl, S., Wernli, H., and Yoshimura, K.: The isotopic composition of precipitation from a winter storm-a case study with the limited-area model COSMOiso, Atmospheric Chemistry and Physics, 12, 1629–1648, https://doi.org/10.5194/acp-12-1629-2012, 2012.

885 Pinzer, B. and Schneebeli, M.: Breeding snow: an instrumented sample holder for simultaneous tomographic and thermal studies, Meas. Sci. Technol., 20, 095705, https://doi.org/10.1088/0957-0233/20/9/095705, 2009a.

Pinzer, B. R. and Schneebeli, M.: Snow metamorphism under alternating temperature gradients: Morphology and recrystallization in surface snow, Geophysical Research Letters, 36, 10–13, https://doi.org/10.1029/2009GL039618, 2009b.

Proksch, M., Löwe, H., and Schneebeli, M.: Density, specific surface area, and correlation length of snow measured by high-890 resolution penetrometry, Journal of Geophysical Research: Earth Surface, 120, 346–362, https://doi.org/10.1002/2014JF003266, 2015.

Pruppacher, H. R. and Klett, J. D.: Microphysics of Clouds and Precipitation, 2nd ed., Kluwer Academic, 1997.

Sato, T., Kosugi, K., Mochizuki, S., and Nemoto, M.: Wind speed dependences of fracture and accumulation of snowflakes on snow surface, Cold Regions Science and Technology, 51, 229–239, https://doi.org/10.1016/j.coldregions.2007.05.004, 895 2008.

Schleef, S., Jaggi, M., Löwe, H., and Schneebeli, M.: An improved machine to produce nature-identical snow in the laboratory, J. Glaciol., 60, 94–102, https://doi.org/10.3189/2014JoG13J118, 2014a.

Schleef, S., Löwe, H., and Schneebeli, M.: Influence of stress, temperature and crystal morphology on isothermal densification and specific surface area decrease of new snow, The Cryosphere, 8, 1825–1838, https://doi.org/10.5194/tc-8-900 1825-2014, 2014b.

Schmidt, R. A.: Vertical profiles of wind speed, snow concentration, and humidity in blowing snow, Boundary-Layer Meteorol, 23, 223–246, https://doi.org/10.1007/BF00123299, 1982.

Sharma, V., Comola, F., and Lehning, M.: On the suitability of the Thorpe–Mason model for calculating sublimation of saltating snow, The Cryosphere, 12, 3499–3509, https://doi.org/10.5194/tc-12-3499-2018, 2018.

905 Sigmund, A., Dujardin, J., Comola, F., Sharma, V., Huwald, H., Melo, D. B., Hirasawa, N., Nishimura, K., and Lehning, M.:
Evidence of Strong Flux Underestimation by Bulk Parametrizations During Drifting and Blowing Snow, Boundary-Layer
Meteorology, 182, 119–146, https://doi.org/10.1007/s10546-021-00653-x, 2021.

Sigmund, A., Melo, D. B., Dujardin, J., Nishimura, K., and Lehning, M.: Parameterizing Snow Sublimation in Conditions of
Drifting and Blowing Snow, JAMES, submitted.

910 Sokratov, S. A. and Golubev, V. N.: Snow isotopic content change by sublimation, Journal of Glaciology, 55,
https://doi.org/10.3189/002214309790152456, 2009.

Sommer, C. G., Lehning, M., and Fierz, C.: Wind tunnel experiments: saltation is necessary for wind-packing, J. Glaciol.,
63, 950–958, https://doi.org/10.1017/jog.2017.53, 2017.

Sommer, C. G., Wever, N., Fierz, C., and Lehning, M.: Investigation of a wind-packing event in Queen Maud Land,
915 Antarctica, The Cryosphere, 12, 2923–2939, https://doi.org/10.5194/tc-12-2923-2018, 2018a.

Sommer, C. G., Lehning, M., and Fierz, C.: Wind Tunnel Experiments: Influence of Erosion and Deposition on Wind-
Packing of New Snow, Front. Earth Sci., 6, 4, https://doi.org/10.3389/feart.2018.00004, 2018b.

Stenni, B., Curran, M. A. J., Abram, N. J., Orsi, A., Goursaud, S., Masson-Delmotte, V., Neukom, R., Goosse, H., Divine,
D., Van Ommen, T., Steig, E. J., Dixon, D. A., Thomas, E. R., Bertler, N. A. N., Isaksson, E., Ekaykin, A., Werner, M., and
920 Frezzotti, M.: Antarctic climate variability on regional and continental scales over the last 2000 years, Climate of the Past,
13, 1609–1634, https://doi.org/10.5194/cp-13-1609-2017, 2017.

Stichler, W., Schotterer, U., Fröhlich, K., Ginot, P., Kull, C., Gäggeler, H., and Pouyaud, B.: Influence of sublimation on
stable isotope records recovered from high-altitude glaciers in the tropical Andes, Journal of Geophysical Research:
Atmospheres, 106, 22613–22620, https://doi.org/10.1029/2001JD900179, 2001.

925 The Firn Symposium team, Amory, C., Buizert, C., Buzzard, S., Case, E., Clerx, N., Culberg, R., Datta, R. T., Dey, R.,
Drews, R., Dunmire, D., Eayrs, C., Hansen, N., Humbert, A., Kaitheri, A., Keegan, K., Kuipers Munneke, P., Lenaerts, J. T.
M., Lhermitte, S., Mair, D., McDowell, I., Mejia, J., Meyer, C. R., Morris, E., Moser, D., Oraschewski, F. M., Pearce, E., De
Roda Husman, S., Schlegel, N.-J., Schultz, T., Simonsen, S. B., Stevens, C. M., Thomas, E. R., Thompson-Munson, M.,
Wever, N., and Wouters, B.: Firn on ice sheets, Nat Rev Earth Environ, https://doi.org/10.1038/s43017-023-00507-9, 2024.

930 Thorpe, A. D. and Mason, B. J.: The evaporation of ice spheres and ice crystals, Br. J. Appl. Phys., 17, 541–548,
https://doi.org/10.1088/0508-3443/17/4/316, 1966.

Town, M., Steen-Larsen, H. C., Wahl, S., Faber, A.-K., Behrens, M., Jones, T., and Sveinbjornsdottir, A.: Post-depositional
modification on seasonal-to-interannual timescales alters the deuterium excess signals in summer snow layers in Greenland,
Snow/Greenland, https://doi.org/10.5194/egusphere-2023-2462, 2024.

935 Uemura, R., Masson-Delmotte, V., Jouzel, J., Landais, A., Motoyama, H., and Stenni, B.: Ranges of moisture-source
temperature estimated from Antarctic ice cores stable isotope records over glacial-interglacial cycles, Climate of the Past, 8,
1109–1125, https://doi.org/10.5194/cp-8-1109-2012, 2012.

Vinther, B. M., Buchardt, S. L., Clausen, H. B., Dahl-Jensen, D., Johnsen, S. J., Fisher, D. A., Koerner, R. M., Raynaud, D.,
Lipenkov, V., Andersen, K. K., Blunier, T., Rasmussen, S. O., Steffensen, J. P., and Svensson, A. M.: Holocene thinning of
940 the Greenland ice sheet, Nature, 461, https://doi.org/10.1038/nature08355, 2009.

Vionnet, V., Brun, E., Morin, S., Boone, A., Faroux, S., Le Moigne, P., Martin, E., and Willemet, J. M.: The detailed snowpack scheme Crocus and its implementation in SURFEX v7.2, Geoscientific Model Development, 5, 773–791, https://doi.org/10.5194/gmd-5-773-2012, 2012.

Wagner, D. N., Shupe, M. D., Cox, C., Persson, O. G., Uttal, T., Frey, M. M., Kirchgaessner, A., Schneebeli, M., Jaggi, M., Macfarlane, A. R., Itkin, P., Arndt, S., Hendricks, S., Krampe, D., Nicolaus, M., Ricker, R., Regnery, J., Kolabutin, N., Shimanshuck, E., Oggier, M., Raphael, I., Stroeve, J., and Lehning, M.: Snowfall and snow accumulation during the MOSAiC winter and spring seasons, The Cryosphere, 16, 2373–2402, https://doi.org/10.5194/tc-16-2373-2022, 2022.

Wahl, S., Steen-Larsen, H. C., Reuder, J., and Hörhold, M.: Quantifying the Stable Water Isotopologue Exchange Between the Snow Surface and Lower Atmosphere by Direct Flux Measurements, Journal of Geophysical Research: Atmospheres, 126, 1–24, https://doi.org/10.1029/2020JD034400, 2021.

Wahl, S., Steen-Larsen, H. C., Hughes, A. G., Dietrich, L. J., Zuhr, A., Behrens, M., Faber, A. -K., and Hörhold, M.: Atmosphere-Snow Exchange Explains Surface Snow Isotope Variability, Geophysical Research Letters, 49, https://doi.org/10.1029/2022GL099529, 2022.

Wahl, S., Walter, B., Bianch, L., Aemisegger, F., and Lehning, M.: Ring wind tunnel experiments - airborne snow metamorphism and stable water isotopes, https://doi.org/10.16904/envidat.494, 2024.

Wakai, F., Yoshida, M., Shinoda, Y., and Akatsu, T.: Coarsening and grain growth in sintering of two particles of different sizes, Acta Materialia, 53, 1361–1371, https://doi.org/10.1016/j.actamat.2004.11.029, 2005.

Walter, B., Huwald, H., Gehring, J., Bühler, Y., and Lehning, M.: Radar measurements of blowing snow off a mountain ridge, The Cryosphere, 14, 1779–1794, https://doi.org/10.5194/tc-14-1779-2020, 2020.

Walter, B., Weigel, H., Wahl, S., and Löwe, H.: Wind tunnel experiments to quantify the effect of aeolian snow transport on the surface snow microstructure, Snow/Snow Physics, https://doi.org/10.5194/tc-2023-112, 2023.

Weng, Y., Touzeau, A., and Sodemann, H.: Correcting the impact of the isotope composition on the mixing ratio dependency of water vapour isotope measurements with cavity ring-down spectrometers, Atmospheric Measurement Techniques, 13, 3167–3190, https://doi.org/10.5194/amt-13-3167-2020, 2020.

Wever, N., Lehning, M., Clifton, A., Rüedi, J.-D., Nishimura, K., Nemoto, M., Yamaguchi, S., and Sato, A.: Verification of moisture budgets during drifting snow conditions in a cold wind tunnel: MOISTURE BUDGETS OF DRIFTING SNOW, Water Resour. Res., 45, https://doi.org/10.1029/2008WR007522, 2009.

Yamaguchi, S., Ishizaka, M., Motoyoshi, H., Nakai, S., Vionnet, V., Aoki, T., Yamashita, K., Hashimoto, A., and Hachikubo, A.: Measurement of specific surface area of fresh solid precipitation particles in heavy snowfall regions of Japan, The Cryosphere, 13, 2713–2732, https://doi.org/10.5194/tc-13-2713-2019, 2019.

Yang, Y., Kiv, D., Bhatta, S., Ganeshan, M., Lu, X., and Palm, S.: Diagnosis of Antarctic Blowing Snow Properties Using MERRA-2 Reanalysis with a Machine Learning Model, Journal of Applied Meteorology and Climatology, 62, 1055–1068, https://doi.org/10.1175/JAMC-D-23-0004.1, 2023.

Yu, H., Li, G., Walter, B., Lehning, M., Zhang, J., and Huang, N.: Wind conditions for snow cornice formation in a wind tunnel, The Cryosphere, 17, 639–651, https://doi.org/10.5194/tc-17-639-2023, 2023.

Zuhr, A. M., Wahl, S., Steen-Larsen, H. C., Hörhold, M., Meyer, H., and Laepple, T.: A Snapshot on the Buildup of the Stable Water Isotopic Signal in the Upper Snowpack at EastGRIP on the Greenland Ice Sheet, JGR Earth Surface, 128, https://doi.org/10.1029/2022JF006767, 2023a.

980   Zuhr, A. M., Wahl, S., Steen-Larsen, H. C., Hörhold, M., Meyer, H., Gkinis, V., and Laepple, T.: Spatial and temporal stable water isotope data from the upper snowpack at the EastGRIP camp site, NE Greenland sampled in summer 2018, https://doi.org/10.5194/essd-2023-136, 18 October 2023b.